THESIS FOR THE DEGREE OF LICENTIATE OF ENGINEERING

Lithium ion Battery Aging: Battery Lifetime Testing and Physics-based Modeling for Electric Vehicle Applications

Evelina Wikner

Division of Electric Power Engineering
Department of Electrical Engineering
CHALMERS UNIVERSITY OF TECHNOLOGY
Göteborg, Sweden 2017

Lithium ion Battery Aging:
Battery Lifetime Testing and Physics-based Modeling for Electric Vehicle Applications

Department of Electrical Engineering
CHALMERS UNIVERSITY OF TECHNOLOGY
SE-412 96 Göteborg
Sweden
Telephone + 46 (0)31 772 00 00

To my family

Abstract

Electrification of vehicles is one solution in reducing emissions from the transport sector, and in particular to limit tail-pipe emissions in cities. In order to make the electrification s uccessful a nd c ost e ffective, t here i s a high demand for longer drive range and longer battery lifetime. By improving the understanding for the underlying aging mechanisms of vehicle lithium ion batteries, the utilization can be improved and thus cost effective.

This thesis contributes with an extensive test matrix for lifetime testing, including calendar and cycling aging, on large commercial cells for automotive applications. The test matrix is constructed to investigate the effect of temperature, C-rate, SOC level, test procedure and DOD. A physics-based model including SEI formation, film r esistance i ncrease a nd l oss o f electrode volume fraction as a function of number of cycles is constructed. Aging parameters were determined through parameterizing the model using calibration experiments.

Lifetime cycling data show that the expected temperature dependence can not be seen for 10% DOD for SOC levels below 50% SOC, it is first for SOC levels higher than 60% that this is observed. Also SOC levels higher than 30% is accelerating the aging, while SOC levels below this show very low aging effects, however, when using cycling in the whole SOC interval, the classical decreased lifetime with higher temperatures were obtained. For cells tested in different DODs, but with the same cut-off voltage, longer lifetime was observed for the small DOD, although the initial aging was similar up to 1200 FCE. After that, the aging decelerated for the small DODs while it accelerated for the large DODs.

Keywords

Electric Vehicle (EV), Plug-in Hybrid Electric Vehicle (PHEV), Hybrid Electric Vehicle (HEV), Battery lifetime tests, Calendar aging, Physics-based modeling

Acknowledgement

I would like to thank my family and friends, for the constant support and encouragement in perusing my goals, this thesis being one of them.

I would especially like to thank my supervisors Prof. Torbjörn Thiringer and Dr. Johan Scheers for there guidance, encouragement and patience.

Also thanks to my colleges at Electric Power Engineering for the open and welcoming working environment, support, and interesting discussions, not always regarding batteries.

Evelina Wikner
Göteborg, June 2017

Preface

This thesis is a result of the project *Aging mechanisms and how to prolong battery life in vehicles and stationary applications* financed by the Swedish Energy Agency, all thanks for the financial support through *Batterifonden*, in collaboration with ABB, Volvo Car Corporation (VCC) and Uppsala University (UU). ABB and VCC has provided battery testing facilities and extensive testing performed by Tomas Tegner, Antonis Marinopoulos, Lukas Migas and Anneli Jedenmalm at ABB and by Johan Lesser and Michael Östrand at VCC. UU has provided expertise in electrochemical systems and of aging mechanisms in batteries through Daniel Brandell and Kristina Edström. Erik Björklund at UU has performed several measurements for proper parametrization of the model and kindly provided images of the materials.

Contents

List of Abbreviations

The following list presents abbreviations that are used throughout this thesis:

LiB	Lithium ion Battery
Li^+	Lithium ion
BOL	Beginning of Life
MOL	Middle of Life
EOL	End of Life
SOH	State–of–Health the ratio of the capacity at any given time over the nominal capacity of a fresh battery
SOC	State–of–Charge (0-100%)
OCV	Open Circuit Voltage
C-rate	X C-rate is the rate at which a battery is completely discharge or charged in 1/X h.
DOD	Depth of Discharge (0-100%)
FCE	Full Cycle Equivalent
CC	Constant Current
CV	Constant Voltage
SEI	Solid Electrolyte Interphase
SPI	Solid Permeable Interphase
PHEV	Plug-in Hybrid Electric Vehicle
HEV	Hybrid Electric Vehicle

EV	Electric Vehicle
OEM	Original Equipment Manufacturer
NMC	Lithium Nickel Manganese Cobalt oxide
LMO	Lithium Manganese Oxide
MO	Metal Oxide
EC	Ethylene Carbonate
DMC	Dimethyl Carbonate
DEC	Diethyl Carbonate
EMC	Ethylmethyl Carbonate
cc	Current Collector
RPT	Reference Performance Test
ICA	Incremental Capacity Analysis
es	Electronic State

List of Symbols

subscript s/l	Solid/liquid material
subscript $+/-$	Li^+/PF_6^-
subscript a/c	Anodic/Cathodic reaction
a_+	Activity
c	Concentration
c_{solv}	Solvent concentration
c_T	Total concentration
C_{dl}	Double layer capacitance
d_{SEI}	SEI thickness
D	Diffusivity
E_{eq}	Equilibrium potential
$f_\pm$	Salt activity coefficient
F	Faradays constant
$\mathbf{i}$	Current density
k	Reaction rate
K	Friction coefficient
$\mathbf{L}$	Length
M	Molar mass
n	Number of electrons

N	Molar flux
r_p	Particle radius
R	Gas constant
R_{film}	Film resistance [Ω/m^2]
S_a	Specific surface area
t_+	Transport number for Li^+
T	Temperature
u	Ionic mobility
$\mathbf{v}$	Fluid velocity
V_m	Partial molar volume
z	Ionic charge
Q_{cell}	Battery capacity
$Q_{a/c}$	Amount of active host material
α	Reaction rate coefficient
β	Bruggeman Coefficient
ϵ	Volume fraction
η	Activation over potential
$\nu_{reactions}$	Reaction product, moles
$\nu_{+/-}$	Number of cations and anions formed when 1 mol electrolyte dissolves
σ	Conductivity of solid material
κ	Conductivity of electrolyte
μ	Electrochemical potential
ϕ	Electric potential
$\Delta\phi_{film}$	Voltage drop over resistive film

Chapter 1

Introduction

1.1 Background

Electrification of vehicles is seen as one of the key solutions in reducing emissions from the transport sector. In particular, the tail-pipe emissions can be reduced, which is very important in some large cities. Today the transport sector is one contributor to air pollution in cities and is responsible for almost a quarter of the total greenhouse gas emissions in Europe [1]. By the end of 2016 there were 28113 electrified vehicles registered in Sweden, 33% pure electric vehicles (EV) and 67% plug-in hybrid electric vehicles (PHEV). The prognosis for the end of 2017 is 48000 vehicles [2].

The by far most common solution for EVs is to use lithium ion batteries (LiBs) for the on board energy storage. As the market for EV, hybrid electric vehicle (HEV) and PHEV is increasing, the demand for longer driving range and lifetime requirement calls for further development, utilization and understanding of the LiBs.

The battery is an expensive component in the vehicle through better understanding of the aging, the usage of the battery in the vehicle can be optimized. An improved understanding could lead to a better estimate of the state of health (SOH) of the battery in the vehicle. Today the warranty time for the battery in EV's varies for different models and manufacturers and is around 8 years or 100 000 miles with 70% capacity degradation [3]. A better understanding for what current and power limits to use for the battery could help prolonging the lifetime, and thereby the warranty time. Physics-based models can be used to improve the understanding for the effect of different usage cases in connection to different aging mechanisms.

The development of physics-based models will require correlation to life-

time testing. The lifetime cycling is time consuming and costly. Improving the test methods used for lifetime cycling is therefore also needed.

1.2 Previous Work

The LiBs are continuously developed and improved, for each new battery chemistry extensive tests have to be performed to be able to estimate the aging during operation. Several empirical [4–6], semi-empirical [7–9] and circuit models [10] have been presented over the years. Very interesting from [4] is the indications of the effects of Stat of Charge (SOC) level used, although this study was done for $LiPO_4$. The downside of these models is that they are parameterized from extensive test matrices. This is an expensive and time consuming task. These models can not simply be coupled to the electrochemical processes occurring in the battery during its lifetime.

To better understand the battery, physics-based models are used to describe the underlying electrochemical processes [8, 11–14]. These models can capture and improve the understanding for the underlying aging mechanism better than the empirical and semi-empirical models. The physics-based models, though, needs mathematical descriptions for the aging mechanisms, for which some have not yet been derived.

There are some different approaches described in the literature on how to simulate capacity fade in batteries. The most common is to simulate parasitic side reactions inducing a resistive film growth and capacity fade due to the resistance increase and loss of lithium ions (Li^+) [8, 11, 12, 15]. Other approaches include that of Spotnitz et al. [16] who developed polynomial expressions from an empirical study, estimating the irreversible and reversible Li^+ loss. There are, however, many more aging mechanisms occurring in the battery during use.

There is a lack of published literature on physics-based modeling linked to cycling aging of large commercial cells. The need for lifetime testing in correlation with physics-based models is a key factor in further developing the understanding for the aging mechanisms. To correlate different aging mechanisms to the battery usage, and use this to better utilize the battery in specific applications.

1.3 Purpose of Work

The purpose of this work is to deepen the understanding of aging phenomena in LiBs. A physics-based aging model is built for a commercial LiB of pouch type. The model describes three linked aging mechanisms using elec-

trochemical equations in combination with experimental aging studies. An aging model capturing the different aging mechanisms can reduce the required test matrix needed for battery characterization. It will also provide a better understanding of the limits in the utilization of the battery for different applications. The aging mechanisms described in this model is capacity fade and resistance increase from side reactions similar to previous work [15]. In the model, the side reactions give rise to loss of recyclable Li^+ and continuous growth of a resistive film on the anode particles. The film growth also reduces the volume fraction of electrolyte in the porous anode.

1.4 Contributions

The contributions made in this thesis are the following:

- The aging consequences for cells tested in 10% intervals of SOC, were quantified at three different temperatures and showed that:
  - SOC intervals lower than 30% can improve cycling lifetime 3x the expected full cycle equivalent (FCE) lifetime.
  - There is a large difference in aging between the different SOC intervals; Low SOC intervals will not reach end of life (EOL) within this project time, while higher SOC ($\geq$50%) reached EOL after approximately 3000 FCE.
  - The importance of temperature for 10% SOC intervals has proven to be small for intervals $\leq$50% SOC in contrast to large depth of discharge (DOD). The results presented here show that a temperature of close to 40°C is more beneficial compared to a lower temperature of 30°C.
  - For SOC intervals above 50% SOC, increasing aging with increasing temperature is observed first above 40°C.
- The effect of Coulomb counting without an upper cutoff voltage limit has been experimentally demonstrated to increase the aging in comparison to constant voltage (CV) charging using an upper cutoff voltage limit.
- The life expectancy for large DOD are confirmed to be shorter in comparison to small DOD, 10% DOD can give more than 2 times longer lifetime. The highest allowed voltage shows to hold a strong correlation to the lifetime where lower SOC levels can prolong the lifetime more than 6 times.

- An electrochemically based aging model was set up for lifetime prediction including loss of recyclable Li^+, resistive film growth, and loss of electrolyte volume in the electrode and base functionalities demonstrated.
- Diffusion coefficient for the mixed cathode material, Lithium Nickel Manganese Cobalt Oxide (NMC)/ Lithium Manganese Oxide (LMO), was estimated for the electrochemically based model from voltage and current measurements on a commercial cell.

Chapter 2

Theory

2.1 Lithium Ion Batteries (LIBs)

LIBs are built up from a number of electrochemical cells. These electrochemical cells can store or release energy through electrochemical reactions, faradaic processes. An electrochemical cell is composed of an anode, a cathode and between them an electrically insulating, but ionically conducting electrolyte enabling ions to move through the cell. There is also a rigid separator, often a polymer, between the anode and cathode to contain the electrolyte and prevent short circuit. Li^+ and other Li based batteries have the highest energy densities, of all existing rechargeable batteries [17].

The electrodes can be of metallic or insertion type. In this thesis only the insertion type electrodes, which are most common for all LiB, are invesitgated. The insertion electrodes have porous structures with large surface areas where the transfer of electrons (redox reactions) between ion and electrode material can occur. The electrodes function as hosts for Li^+ [18].

In the charged state the anode (negative electrode) has a high concentration of lithium and low potential. The cathode (positive electrode) has a low concentration of lithium and high potential. When connecting the electrodes via an external load electrons move spontaneously from the anode, increasing its potential, through the load to the cathode, decreasing its potential, therefore reducing the driving force, i.e the overall cell voltage. Li^+'s are simultaneously transported by the electrolyte from the anode, through the separator, to the cathode to conserve charge neutrality, figure 2.1. The described processes are that of a discharge. The processes are reversed during charging of the battery [17]. The reactions occurring in the batteries during charge an discharge are;

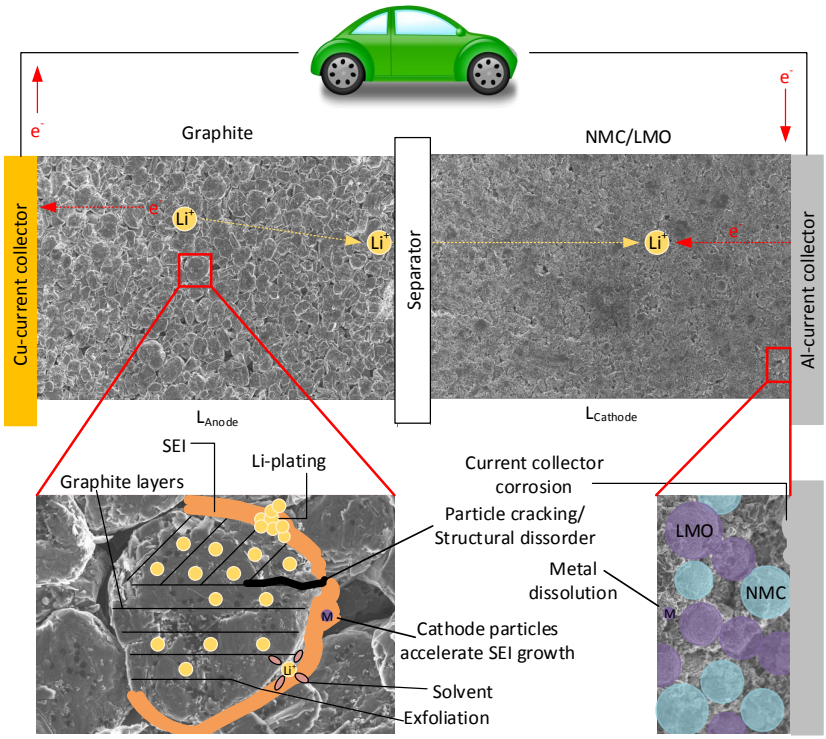

Figure 2.1: Schematic illustration of how a LiB works during discharge and the aging mechanisms that can occur during usage [19].

Anode:

$$Li_xC_6 \rightleftharpoons xLi^+ + xe^- + C_6$$

Cathode:

$$Li_{1-x}MO + xLi^+ + xe^- \rightleftharpoons LiMO$$

Overall cell reaction:

$$Li_xC_6 + Li_{1-x}MO \underset{charge}{\overset{discharge}{\rightleftharpoons}} C_6 + LiMO$$

where MO denotes an arbitrary metal oxide and $0 \leq x \leq 1$ [20, 21].

The Open Circuit Voltage (OCV) is the voltage over the cell when no load is applied and is a function of the SOC of the cell. The SOC itself is a

linear function of the total capacity of the cell and is specified by a limited voltage interval, determined so that the electrode materials and electrolyte are stability during cycling [18]. The 0% and 100% SOC level of the cell does not have to correspond to the minimum and maximum possible cell voltages. By operating in a limited voltage window, where the end points are defined as 0 and 100% SOC, the reversibility of the reactions and lifetime of the cell is improved. An example of how the cell OCV vs SOC is a combination of the anode and cathode material potentials can be seen in figure 2.2.

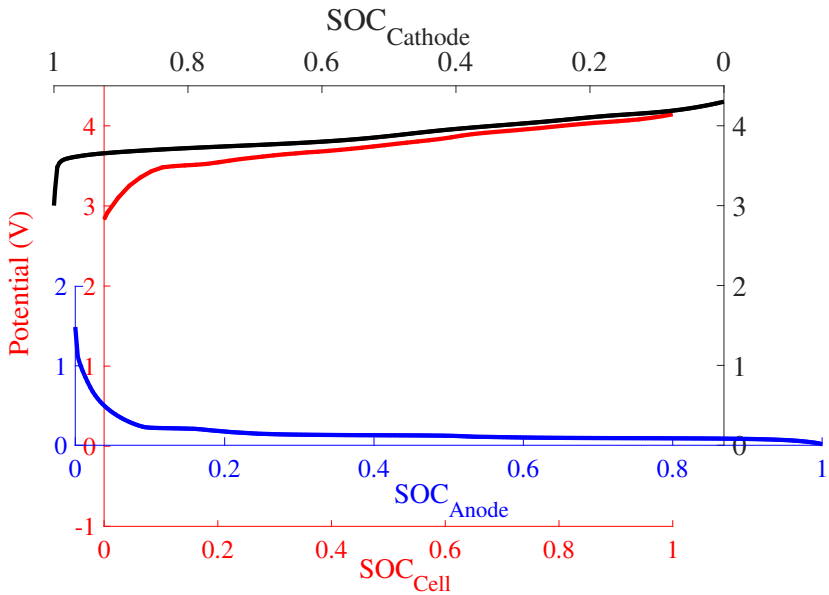

Figure 2.2: Cell OCV curve and the electrode materials potential as a function of respectivly SOC.

The energy output of the battery of course depends on the operating voltage and storage capacities of lithium in the electrode materials, thus there is a balance between energy output and battery longevity decided by the usage of the battery. For the electrode reactions to occur there has to be an overpotential that drives the reactions, this leads to a decrease in the battery voltage, with respect to the OCV, as a result of the internal resistance. If the cell is to provide high power, the discharge process has to be rapid, and the internal resistance low. At high current rates the internal resistance will increase and result in a larger change in voltage. Other properties that lowers a battery's energy output include ohmic losses from the electrical resistance of the electrolyte and resistance in the electrodes and current collectors.

Commercial batteries uses anodes of carbonaceous materials, most commonly graphite. The gravimetric capacity of graphite is typically 360-365 mAh/g, close to the theoretical value of 372 mAh/g (LiC_6).

Cathodes are made of metal oxides, mixed layered oxides or phosphates including one or several transition metal ions such as Cobalt, Manganese, Nickel or Iron. The capacities obtainable from the cathode material are limited to the amount of Li^+ they can release and still remain a stable structure. For most cathode materials the lattice contracts as the lithium is deintercalated. The cathode materials typically have theoretical capacities of 150-278 mAh/g and specific capacities of 100-200 mAh/g [22]. This lower capacity of the cathode compared to the anode is compensated for by using more cathode material [17].

Cell Impedance:

The impedance in the battery consists of impedance contributions from several sub-components and the connection between these sub-components. If considering only the major parts, the current collectors (cc) and separator can be modeled as pure resistive components while the porous electrodes are more complex. The impedance in the electrodes consists of contact resistance, charge transfer and diffusion. The contact resistance describes how good the contact is between electrode particles and between electrode and cc, which may also include the conductivity of the solid particles. The charge transfer impedance describes the reaction kinetics, double layer capacitance and transport of Li^+ through the surface film, Solid Electrolyte Interphase (SEI) or Solid Permeable Interphase (SPI) [10]. The SEI layer on the anode creates an increasing resistance in the Li^+ flow and thereby the charge transfer resistance and total impedance of the anode. This impedance increases with charge rate, cycle number, temperature and particle size of the anode material [23]. An increased SEI layer affect the anodes intercalation and deintercalation kinetics and result in an increase in impedance [19].

2.2 Aging Processes

Batteries degrade as they age, they experience power and energy fade associated with impedance rise and capacity loss. The capacity loss can be linked to degradation of the electrolyte components through side reactions with Li^+ with the result of less cyclable Li^+ and in the electrodes by loss of active electrode material. The power losses are consisting of contact resistance in interphases between the materials, growth of resistive film on the active material, loss of active surface area and impaired mass transport [24]. The different components of the battery experience different aging processes.

The cc often experience corrosion and the separator can melt and change shape at high temperatures, mechanical damage from other components on the separator is also be possible. The binder and electrolyte decomposes by electrochemical and chemical reactions accelerated by high temperatures, high and low electrode potentials. The active electrode materials can experience structural disorder, cracking of particles, surface film formation and in the cathode material metal dissolution can occur [25].

2.2.1 Calendar and Cycling Aging

The cells are aging even when they are not used. Depending on the ambient temperature and SOC of the battery the aging is more or less severe. Higher SOC and higher temperature gives more severe aging [6, 19]. In PHEV and EV a considerable part, 20-30% [26], of the aging are from the calendar aging occurring when the vehicle is not used. According to [27], a personal vehicle is only used for 3% of the time. The main aging process contributing to the calendar aging is SEI growth on the anode, Section 2.2.2 [28]. Metal dissolution from the cathode material and migration to the anode material is another contribution, Section 2.2.3. The positive metal ions contributes to faster growth of the SEI layer and decomposition of the electrolyte [29].

When using the battery, the severity of the aging is depending on the load the battery is exposed to and the battery temperature. High currents and high temperatures are detrimental for the battery. To utilize the battery in an application, a balancing between DOD, maximum load and desired lifetime of the battery has to be made [10].

2.2.2 Anode Aging Mechanisms

The anode materials micro-structure, texture, crystallinity and morphology directly influence its performance. The anode electrode has an excess capacity compared to the cathode. Even so the area of the anode has to be larger than the cathodes in order to prevent edge lithium plating and to be able to deliver higher energy density. If the anode capacity is reduced too much, the risk of polarizing it to a potential close to lithium deposition potentials, 0 V vs Li/Li^+, increases. High surface area of the electrode is preferred since it gives a shorter diffusion path for Li^+, faster charge and discharge rate and improves the capacity of the battery [23]. The main aging mechanisms that can occur in the anode are SEI formation, contact loss and loss of active material, figure 2.1) [19].

SEI Formation:

The first time a battery is cycled, the electrolyte and graphite anode will react forming a passivated surface layer called solid electrolyte interphase (SEI). Different electrolytes promote different reactions. Electrolytes including $LiPF_6$ and organic solvents such as Ethylene Carbonate (EC), Dimethyl Carbonate (DMC) or Diethyl Carbonate (DEC) cause formation of species like Li-alkyl carbonates, $ROCO_2Li$, and Li carbonate, $LiCO_3$, on the anode surface [23]. At higher battery potentials the graphite anode oxidises during the intercalation of Li^+ into the anode particles. At these potentials electrolyte solvents reacts with Li^+ and the reaction products precipitate on the anode surface increasing the thickness of the SEI layer, which in turn slows down the intercalation process [23]. The positive ions, cations such as Mn^{2+} or Co^{2+} from the cathode material, contaminates the anode surface by forming oxides and hinder the intercalation process [30].

The thickness of the SEI layer is a function of operating cycles, temperature and materials. During intercalation/deintercalation the graphite expands and contracts and with increasing numbers of cycles it can become unstable and crack. This in turn leads to further surface reactions forming a thicker SEI layer that may eventually isolate the graphite particles from the cc. The formation of these layers are the predominant source for the loss of Li^+ during storage conditions [23]. The loss of contact between the active particles, and between particles and the cc leads to impedance increase and loss of active material [19].

Loss of Cyclable Li^+:

The loss of cyclable Li^+ mainly are from side reactions forming SEI and SPI, Section 2.2.3, layer through decomposition of electrolyte compounds binding Li^+. It is the loss of recyclable Li^+ at the anode that is the major cause of the reduced capacity of the battery [23]. The decomposition of electrolyte usually starts below 0.8 V vs Li/Li^+ [31].

Metallic Li-plating on the Anode:

Metallic Li-plating on the anode is to some extent reversible. Factors that initiate the formation of metallic Li on the anode electrode surface are; the nature of the electrolyte, the ratio between anode and cathode capacities, the operating temperature and charge rate.

For graphite electrodes the close proximity of its reversible potential to Li/Li^+ is making it more susceptible to Li-plating. When the potential of the anode becomes close or equal to the Li-plating potential (0V vs Li/Li^+) it is

favorable for Li^+ to form metallic dendrite on the surface of the anode rather than intercalating into the carbon lattice. The risk of dendrites are higher at low temperature and high charge current. Dendrites can cause the separator to disconnect (lose contact with the electrolyte) and even pierce through it, causing a short circuit and thermal runway in the battery. Li-plating usually manifests itself as a voltage plateau on the discharge voltage profile and low columbic efficiency [23].

Structural Changes:

The structural changes in the anode material when cycling the battery is not the main, but an additional contributor to battery degradation. Cycling the battery at high currents induces mechanical strain on the graphite lattice and steep gradients of Li^+ in the material. The insertion and de-insertion of Li^+ induces mechanical stress that with time will cause the particles to crack and split, making them less ordered compared to the original structure [23]. The expansion and cracking of particles enables further SEI growth that accelerates the aging, this can also lead to loss of active material [19]. The geometry of the graphite particles effects the reversible capacity. Pressed particles with less oriented graphite particles have low reversible capacity. The intercalation kinetics becomes more difficult and new boundaries are created between crystallites where irreversible Li^+/electrolyte interaction can occur [23].

2.2.3 Cathode Aging Mechanisms

The degradation in the composite cathode materials can be separated into two main effects, film-formation and loss of active material [32]. Other mechanisms are structural changes, degradation or change of binder and conducting agents [19].

SPI Formation:

The film layer formed on the cathode particles are called Solid Permeable Interphase (SPI) and, therefore, distinguished from the anode SEI because of its different composition and properties [33]. The SPI is formed on the electrode particles from reactions with electrolyte components and similar to the SEI layer it undergoes changes during the batteries entire lifetime. The SPI thickness is a few nm and consists of both inorganic and organic species. The organic species formed is commonly LiF, Li_xPF_y and $Li_xPF_yO_z$. Which inorganic species that is formed, is dependent on the cathode material and electrolyte. The thickness of the SPI also increases with cycle number,

storage time and significantly with temperature [34].

Loss of Active Material:

The loss of active material can come from structural changes, particle cracking, metal dissolution and loss of contact to the cc. Structural changes can appear when metal in the cathode material dissolves in the electrolyte, as described in Section 2.2.2.

Metal Dissolution:

Metal dissolution from the cathode material causes capacity loss and give rise to a higher contact resistance at the metal depleted interface. For some cathode materials these metal ions can form isolating precipitates on the cathode surface leading to increasing impedance [19]. The resistance for the intercalation/deintercalation reaction has also been seen to increase. In LMO based cells, the Mn^{2+} dissolution increase with the lithium content in the cathode, i.e at high potentials, especially above 4.1 V vs Li/Li^+ [29]. The metal dissolution can lead to further aging by migrating to the anode causing reactions on the anode surface (see Section 2.2.2) [35].

2.3 Mathematical Formulation of Electrochemical Processes

The most commonly used and established mathematical method for physics-based simulations of LiBs is the so called Fuller, Doyle and Newman theory, often referred to as the Newman model.

The model describes the behavior of both solid and liquid phases using concentrated solution theory and porous electrode theory. It describes the one-dimensional transport of lithium from one porous electrode through the separator and in to the other porous electrode [13].

In this section an introduction to some fundamental electrochemistry from [36] focusing on the transport of ions in electrolytic systems will be presented.

2.3.1 Mass Transport

Mass transport of ionic species takes place by diffusion, migration and convection. Diffusion is driven by the gradient of chemical potential, the concentration gradient. Migration is driven by the gradient of electric potential and convection by macroscopic streams in the fluid. The total molar flux of a

species, N_T, passed over an arbitrary unit area, can be expressed as the sum of the flux contributions from migration (N_m), diffusion (N_d) and convection (N_c)

$$N_T = N_m + N_d + N_c \tag{2.1}$$

since they are considered independent of each other. In the general expression for transport of matter in electrochemical systems

$$N_T = -z_i u_i F c_i \nabla\phi - D_i \nabla c_i + c_i \mathbf{v} \tag{2.2}$$

where z_i is the ionic charge of species i, u_i the ionic mobility, F Faradays constant, c_i the concentration, ϕ the potential, D_i the diffusion coefficient and $\mathbf{v}$ the fluid velocity.

In the immediate vicinity of the electrode there is no convection due to friction forces at the material surface. In this area diffusion is most effective and it is therefore known as the diffusion layer. At increased distance from the electrode there is no concentration gradient and therefore no diffusion, here convection becomes more important. Mass transport by migration takes place in both of these areas [36].

Conservation of Mass

To simulate the behavior of an electrochemical system it is often necessary to include one or more of the conservation equations for, mass, energy and momentum. The conservation of mass of species i in a volume element with time t is formulated as

$$\frac{dc_i}{dt} = -\nabla \cdot N_T + \sum_{reactions} \nu_{i,reactions} \tag{2.3}$$

where ν_i is moles of species i produced or consumed by reactions [36].

Transport in Eelectrolyte

The driving force for the mass transfer in concentrated solution theory is the gradient in electrochemical potential

$$c_i \nabla \mu_i = \sum_{j \neq i} K_{ij}(\mathbf{v}_j - \mathbf{v}_i) = \sum_{j \neq i} \frac{c_i c_j}{c_T D_{ij}} RT\,(\mathbf{v}_j - \mathbf{v}_i) \tag{2.4}$$

where μ_i is the electrochemical potential, K_{ij} the friction coefficient between species i and j, R the gas constant and T temperature [36]. In a binary electrolyte i and j can be refereed to as $+$ and $-$. By the Gibbs-Duhem equation ($\sum_i n_i d\mu_i = 0$) this results in two independent transport equations.

Using the solvent as reference and setting its velocity to zero the two transport equations in the form of (2.4) are inverted to receive the equations for the molar flux of respectively species

$$\mathbf{N}_+ = -\nu_+ D \nabla c + \frac{\mathbf{i} t_+^0}{z_+ F} \tag{2.5}$$

and

$$\mathbf{N}_- = -\nu_- D \nabla c + \frac{\mathbf{i} t_-^0}{z_- F} \tag{2.6}$$

where $\mathbf{i}$ is the current density, $t_\pm^0$ the transport number and $\nu_{+/-}$ the number of ions formed when 1 mol electrolyte dissolves [13].

Chapter 3

Experimental Setup

In this chapter the test object specifications are presented, as well as the setup for the lifetime cycling, calendar aging and different characterization tests. The result from the characterization measurements performed for model parameters are presented together with measurement methods for analyzing the cell aging.

3.1 Test Object

The test object of this thesis is a commercial 26 Ah Li^+ pouch cell, shown in figure 3.1a. The cell is made up of 13 stacked bicells resulting in a total of 38 electrochemical cells, a simplified schematics is shown in figure 3.1b. The cell is designed for use in the voltage window 2.8-4.15 V, corresponding to 0 and 100% SOC respectively. The current needed to discharge the cell in 1 h is 26 A, 1C-rate. The negative electrode (anode) is surface treated natural graphite and the positive electrode (cathode) is a mixture of spinel LMO (30wt%) and layered NMC (70wt%). The separator is made of Poly propylene and the electrolyte is composed of the solvents EC/DMC/Ethylmethyl Carbonate (EMC) and the salt $LiPF_6$.

The anode reaction is described in Section 2.1 and the two cathode reactions of the mixed electrode are derived from [20]:

NMC:

$$Li_{1-y}Ni_{1/3}Mn_{1/3}Co_{1/3}O_2 + yLi^+ + ye^- \rightleftharpoons LiNi_{1/3}Mn_{1/3}Co_{1/3}O_2$$

LMO:

$$Li_{1-z}Mn_2O_4 + zLi^+ + ze^- \rightleftharpoons LiMn_2O_4$$

(a)

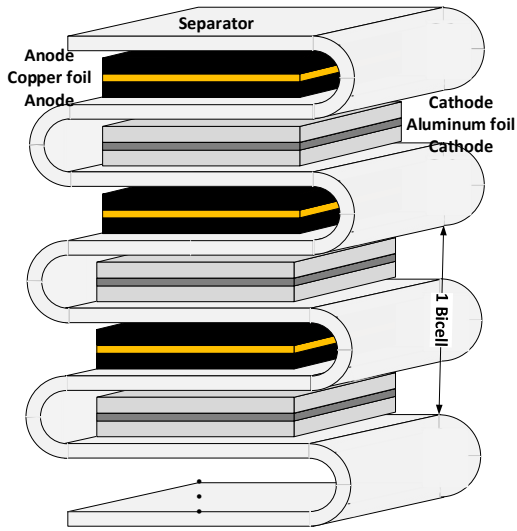

(b)

Figure 3.1: (a) The test cell and (b) a simplified picture of its composure. The internal structure of a single cell is composed of multiple electrodes stacked with the separator in a zigzag pattern. One bicell consists of electrode sheets sandwiched with anode/cathode/anode or cathode/anode/cathode.

Overall cell reaction:

$$xLiC_6 + Li_{1-z}Mn_2O_4 + Li_{1-y}Ni_{1/3}Mn_{1/3}Co_{1/3}O_2$$

$$\overset{discharge}{\underset{charge}{\rightleftharpoons}}$$

$$Li_zMn_2O_4 + Li_yNi_{1/3}Mn_{1/3}Co_{1/3}O_2 + C_6$$

where $x = y + z$, $0 < y \leq 1$ and $0 < z \leq 1$.

3.1.1 Model Parameters

To be able to make a physics-based model of the battery a large number of material parameters are required, some can be taken from literature and others are required to be measured. Therefore several measurements were performed to parameterise the model.

The parameters used in the electrochemical model are given in Tables 3.1, 3.2 and 3.3. For a detailed description of each parameter see Chapter 4 and List of Symbols. The parameters collected from literature are recognized by the source. Parameters measured, estimated or calculated are noted by m, e and c respectively. Measurements performed at Uppsala University are denoted UU.

Table 3.1: Parameters for the cc and porous electrodes used in the simulations.

Parameter	Cathode	Anode	Source
Thickness, L_s (μm)	74	64.5	m UU
L_{cc} (μm)	20	10	m UU
Capacity (mol/m^3)	34150	31507	c from [37]
Volume fraction electrodes (ϵ_s)	0.441	0.57	c
Additives (ϵ_{add})	10-20% of ϵ_s	7-10% of ϵ_s	c from m at UU
Particle radius, r_p (μm)	10/2	17/2	Manufacturer
Diffusivity D_s (m^2/s)	1x10^{-14}-1x10^{-15}	1x10^{-13}-1x10^{-15}	e & [38]
Conductivity σ_s (S/m)	100	100	COMSOL
σ_{cc}	3.546e7	5.998e7	COMSOL
Bruggeman constant electrode, β_s	1.5	1.5	[39]
β_l	3	2.5	e from [40] and [41]
$\alpha_{a/c}$	0.5	0.5	[8]
$k_{a/c}$ (m/s)	5x10^{-10}	1x10^{-10}	

Table 3.2: Cell and electrolyte parameters used in the simulations.

Parameter	Value	Source
T (°C)	25	
Q_0 (Ah)	26	m
i_{1C} (A/m^2)	24.14 A/m^2	c
C_{dl} (F/m^2)	0.2	COMSOL
L_{sep} (μm)	16 um	Manufacturer
c_l (mol/m^3)	1000	Manufacturer
D_l (m^2/s)	3x10^{-10}	COMSOL
$\kappa_l(c_l)$ (S/m)	0.05-1	COMSOL
$\beta_{l,sep}$	3	[40]
$V_{m,salt}$ (m^3/mol)	59x10^{-6}	[40]
$V_{m,solv}$ (m^3/mol)	88x10^{-6}	[40]

Table 3.3: Model parameters used for the SEI layer growth.

Parameter	Value	Source
$E_{eq,SEI}$ (V)	0.4	[8]
$i_{0,SEI}$ (A/m^2)	1.4x10^{-7}	e
κ_{SEI} (S/m)	1x10^{-4}	
ρ_{SEI} (kg/m^3)	2100	[8]
M_{SEI} (kg/mol)	0.073	[8]
$d_{0,SEI}$ (nm)	1	-
$D_{l,SEI}$ (m^2/s)	2.5x10$^-$16	e

3.1.2 Electrode Materials Potential

The anode and cathode potentials, as a function of the Li^+ concentration, were measured at UU in half cells using lithium metal as counter electrode. The electrode potentials can be seen in figure 3.2b and 3.2a as a function of SOC. The definition for SOC in this thesis is the lithium concentration divided by the maximum lithium concentration for respectively material.

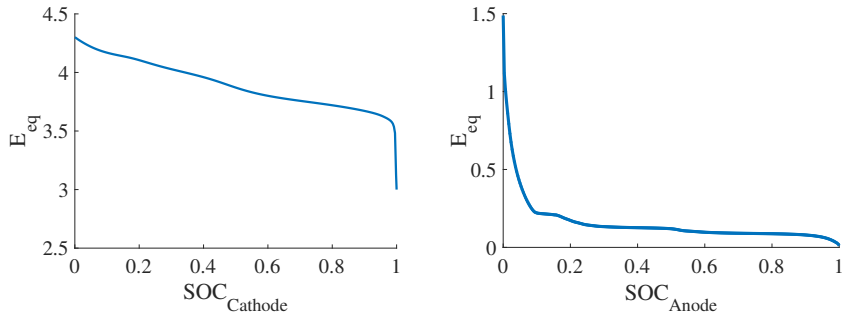

(a) (b)

Figure 3.2: Measured equilibrium potential curves for (a) cathode and (b) anode equilibrium potential as a function of the SOC.

3.2 Cell Aging Tests

To study the aging, calendar and cycling aging were performed. Cycling tests were made for different current rates and SOC intervals. The aging was investigated at four different temperatures by cycling in climate chambers set to 25, 35, 40, and 45°C. The actual cell temperatures during cycling were higher than the chamber temperature due to the heat produced by the cell. Each cell had a temperature sensor to track temperature and ensure safety at all times.

3.2.1 Calendar Tests

The calendar aging is performed by storing the cell at a specified temperature and SOC. Every 30^{th} day a Reference Performance Test (RPT) is performed at 25°C in a dedicated chamber to assess the cell capacity, resistance and self discharge. The cell is then returned to the climate chamber for storage and the process repeated. A total of 18 cells are calender aged under nine unique

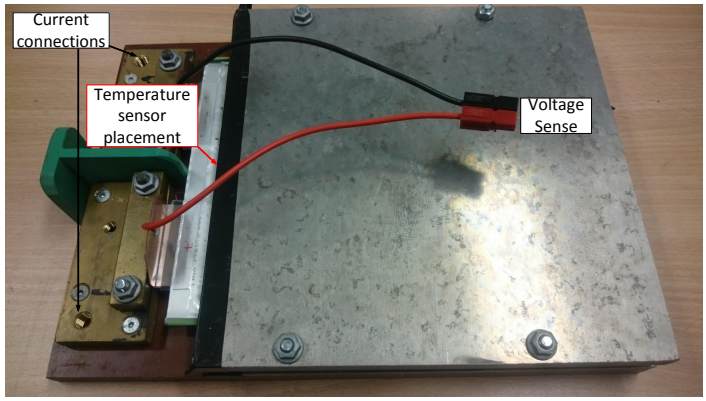

Figure 3.3: Test jig for imitating conditions in a cooled battery pack.

conditions (one replica per test) at 25, 35 or 45°C and at either 15, 75 or 90% SOC.

3.2.2 Lifetime Cycling Tests

The lifetime cycling tests were performed in conditions similar to those in a battery pack in a vehicle. The cell was placed in a specially designed holder or jig, figure 3.3, with limited space to expand. The thick aluminum plate also works as a cooling system with forced airflow on one side. All tests were performed in temperature controlled chambers, Vötsch VT3 7034, VT3 4060 and Clima Temperatur System (CTS), T-40/350. The chamber temperatures were set to 25, 35, 40 or 45°C. The cell cycling equipment used in the project were the following: Maccor Series 4000, PEC SBT0550 and Digatron MCT 100-05-8.

The voltage was measured over the tabs via two bent copper plates pressed together with the tabs by two brass bricks each held in place with two screws. The current connections was done with circular connections to the larger brass blocks. A temperature sensor is placed between the tabs on the cell-body next to the gas-pocket. The temperature difference in the cell is smaller than 4 °C.

When performing aging cycling it is important to have a good control system to ensure that the cycles reflect the intended test. In addition it is also important to ensure safe test conditions. The cycling program should stop the testing before something goes wrong. Apart from health risks, months of testing and expensive equipment are at risk. Each test program includes therefore global limits for temperature, voltage and current so that the test

is terminated and damages avoided in case of a malfunction.

3.2.3 Test Protocols and Load Cycles

The aging tests were performed for different load cycles, temperatures and different DOD. The full test matrix can be seen in Table 3.4. The DOD used are 90%, 80%, 60% and 10%. At intervals $\geq$60% an upper voltage limit combined with Ah-counting were used to maintain the targeted SOC interval, figure 3.4a. In the 10% SOC intervals, Ah-counting was used together with a control method developed at VCC [42], shortly described in Section 3.2.4 (figure 3.4c, 3.4d and 3.4e).

The main current levels tested were 1, 2 and 4C at three different temperatures (25, 35 and 45 °C). Tests were also performed to study the effects of a dynamic current load compared to constant current (CC) load. A drive cycle, Hyzem Rural (figure 3.5), with 2C RMS current was included to be compared with the CC 2C cycle at 80% DOD, for this purpose.

Table 3.4: The test matrix for the lifetime cycling and calendar aging. The superscripts refers to the figure in which data from the respectively test are presented.

Symmetric cycles, SOC [%]	T=25°C			T=35°C			T=45°C		
	1C	2C	4C	1C	2C	4C	1C	2C	4C
0-10		x$^{5.8a}$			x$^{5.8b}$			x$^{5.8c}$	
10-20	x	x$^{5.3a,5.8a}$	x	x$^{5.6a}$	x$^{5.3a,5.6a,5.8b,5.13a}$	x$^{5.6a}$	x	x$^{5.3a,5.8c}$	x
20-30		x$^{5.8a}$						x$^{5.8c}$	x
30-40									
40-50		x$^{5.3b,5.8a}$			x$^{5.3b,5.8b,5.13b}$			x$^{5.8c}$	
50-60									
60-70	x	x$^{5.3c,5.8a}$	x	x$^{5.6b}$	x$^{5.3c,5.6b,5.8b,5.13c}$	x$^{5.6b}$		x$^{5.3c,5.8c}$	x
70-80		x$^{5.8a}$						x$^{5.8c}$	
80-90		x$^{5.8a}$						x$^{5.8c,5.9}$	
80-90 CC-CV		x						x$^{5.9,5.10}$	
0-90		x$^{5.2,5.12a}$			x$^{5.2,5.12b}$			x$^{5.2,5.10,,5.12c}$	

							T=45°C			
							1C	2C	3C	4C
20-80							x$^{5.4,5.5}$			
20-80								x$^{5.5}$		
20-80									x$^{5.5}$	
20-80										x$^{5.5}$

Asymmetric cycles +C-rate, SOC [%]							1C	2C	3C	4C
1C, 10-90		x$^{5.7}$						x$^{5.7,5.11}$		
1C -Hyzem, 10-90		x$^{5.7}$						x$^{5.7}$		
1C, 20-80								x$^{5.4}$		
1C, 20-80									x$^{5.4,5.14a}$	
3C, 20-80										

Calendar Aging[5.1] SOC[%]	T=25°C			T=35°C			T=45°C		
	15	75	90	15	75	90	15	75	90
	x	x	x	x	x	x	x	x	x

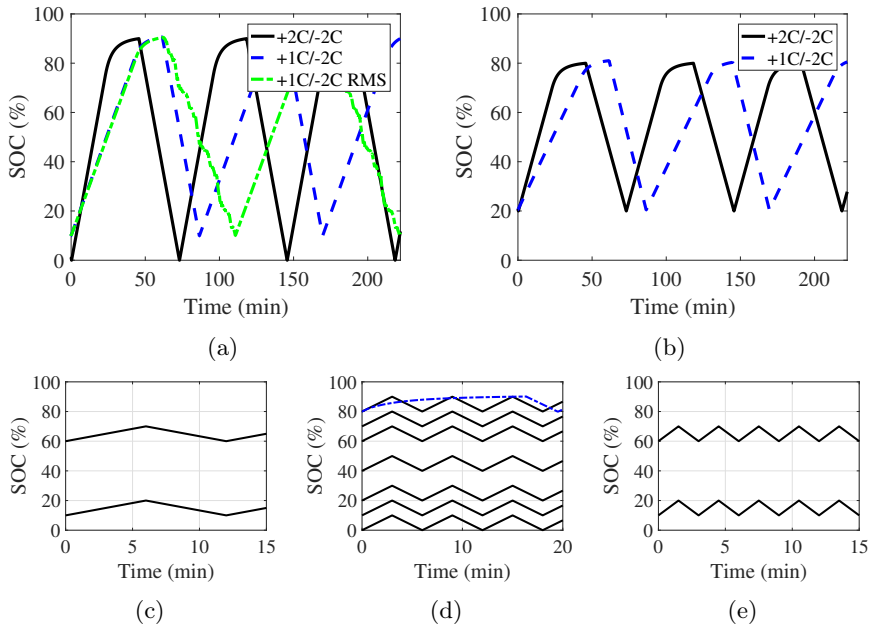

Figure 3.4: Load cycles used for the lifetime cycling, (a) in > 60% DOD, 0-90% +2C/-2C black solid line, 10-90% +1C/-2C blue dashed line and green dashed dotted drive cycle with 1C charge current and 2C RMS discharge current. (b) 60% DOD (20-80% SOC), symmetric, +2C/-2C black solid line, and asymmetric, +1C/-2C blue dashed line. 10% DOD for symmetric +XC/-XC in different SOC intervals (c) 1C, (d) 2C with blue dashed line representing CC-CV at 80-90% SOC, and (e) 4C.

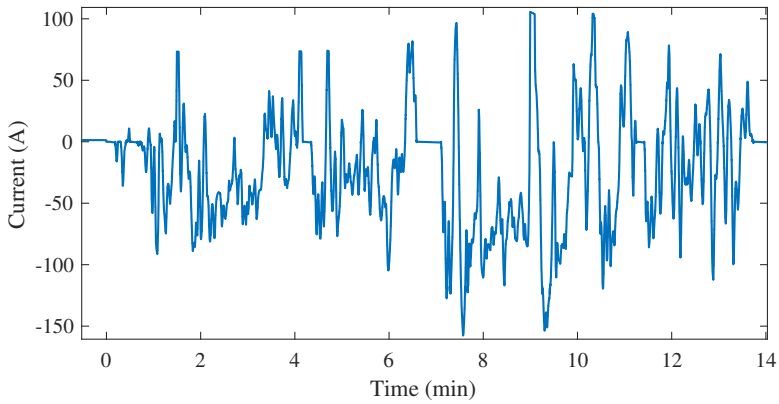

(a)

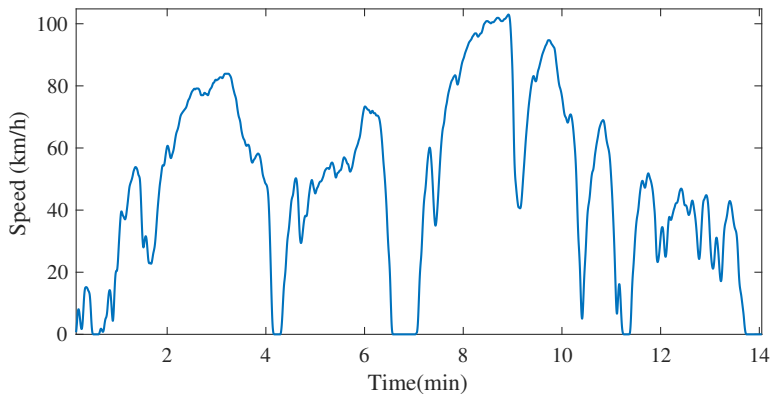

(b)

Figure 3.5: Hyzem Rural (a) current and (b) speed profile [43].

3.2.4 Control Method for 10% SOC Intervals

To control the SOC interval during cycling in 10% DOD with CC, voltage peak and minimum values was used together with Ah-counting. The cell was first discharged to the OCV value for the upper SOC level. In the initiation of the cycling, a control cycle was introduced with CC discharge and charge using Ah-counting, where the end voltage values were stored in two control variables. After each charge and discharge the end voltage value was compared to the voltage value from the control cycle according to

$$\Delta V = |V_{upper/lower,1} - V_{upper/lower,n}| < V_{limit}. \tag{3.1}$$

If ΔV is within a predetermined limit value, V_{limit}, the cycling proceeds. If not a correction cycle of CC-CV is performed to the OCV value for the upper SOC level. The next coming cycle is then the new control cycle.

V_{limit} was adjusted with respect to C-rate, SOC and resistance to ensure a fault tolerance of max 1% SOC. In the low SOC levels a higher value of V_{limit} was allowed due to the shape of the OCV and higher resistance.

$$10 < V_{limit} < 100mV$$

As the resistance increased during aging the limit was increased. At 0% SOC a constant voltage limit of 2.8V was used [42].

3.3 Characterization Tests

Capacity and current pulse tests were performed to track the capacity and resistance changes of the cell during the aging process. Initially these tests were performed every 100 full cycle equivalent (FCE), but less frequent at every 200-1000 FCE after 800 FCE. The periodicity of these tests were adapted for each load profile.

3.3.1 Reference Performance Test (RPT)

The RPT is constructed to measure the capacity, charge and discharge resistance for two different current pulses, 5C for 10s and 1C for 40s in 10% steps over the entire SOC window, figure 3.6a. From these tests more information on the aging taking place in the cell can be extracted by studying the changes in the incremental capacity analysis (ICA) (see Section 3.4.1).

3.3.2 Capacity Test

In periods and test regimes where the cell was expected to change performance rapidly over number of cycles, a capacity test was used in between

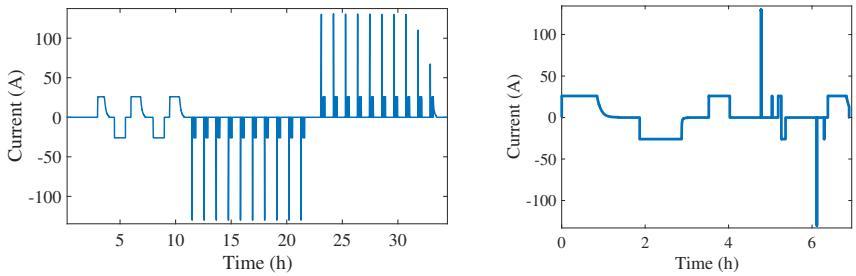

(a) (b)

Figure 3.6: (a) Reference performance test (RPT) for the characterisation of the cell capacity and resistance and (b) Simple RPT for improved continuity in the cycling.

RPT. This was done in order to assure that the test proceeded in the targeted SOC interval. The capacity test was performed in 25°C and consisted of the two initial full cycles of the RPT.

3.3.3 Simple RPT

A simple RPT was developed to be used in the test regimes that showed to be less detrimental to the cell than expected. The simple RPT, figure 3.6b, is consisting of one full cycle measuring the capacity and two charge and discharge pulses of 10s 2C and 40s 1C at 50% SOC with the purpose of tracking the resistance. It was performed at the cycling temperature and incorporated in the cycling protocol. This increased the continuation of the cycling and introduced less handling of the cells.

3.4 Aging Characterization

3.4.1 Incremental Capacity Analysis (ICA)

The incremental capacity can be used to study the batteries aging during lifetime tests. It is a method to evaluate changes in the electrochemical properties of the cell, such as the relative aging of the electrodes. By studying the intensity and position of the peaks, the capacity degradation resulting from loss of Li^+ or active material can be detected together with effects of polarization [10, 44]. The charge and discharge profiles are used to identify the phase equilibrium of the active materials corresponding to plateaus in the voltage profiles. A peak in the ICA corresponds to a phase change in the

intercalation material where two or more phases with different lithium concentrations coexist with the same chemical potential [18, 45]. The differential capacity ($\Delta Q/\Delta V$) is analyzed as a function of the cell potential.

The results depend on the charge and discharge current rate. A slow rate should be used to limit the effects from polarization. For this project 1C has been used to follow the changes in the cells during the aging. At this current the effects of polarization can be clearly seen. To achieve a more unambiguous picture, C/10 is required, but 1C can still provide a crude image of what processes are occurring. Reference ICA on half cell data were used to analyze the peaks in the full cell ICA performed at VCC.

Half Cell ICA

Small pieces of electrode material were taken from a fresh commercial cell and assembled in lab scale pouch cells with a lithium metal counter electrode. The cells were then cycled at a rate of C/28. The peaks in figure 3.7 correspond to phase transitions in respectively electrode material.

The anode shows three clear peaks and two diffuse, figure 3.7b. The Li^+ intercalation occurs step wise, in a so called stage formation. Li^+ is intercalated between the graphene layers separated by a number of empty layers. The step index, s, identifies the number of layers between occupied layers. It is energetically favorable to completely fill one layer before a new layer starts to be filled. The phase at the beginning of the lithiation is known as stage V, $0 < x \leq 0.166$ lithium intercalated in LiC (Li_xC_6). Peak 5 represents the phase transition to stage IV. The small Peak 4 represents the change from stage IV to III ($0.166 < x \leq 0.22$). Peak 3 ($0.22 < x \leq 0.34$) represents the transition from stage III to II L and Peak 2 from stage II L to II, $0.34 < x \leq 0.5$. The difference between stage II L and II is due to different Li^+ packing densities. Finally Peak1 is due to the transition to stage I ($0.5 < x \leq 1$) [20, 45, 46].

The ICA for the cathode includes three distinct peaks, figure 3.7a. Peak 1 is the contribution from NMC [32,47]. The hexagonal layered structure is not changed during charge and discharge but a phase transformation mechanism linked to changes in the electronic state (es) occur (hybridization of Co and O orbitals) [48]. Peak 2 and 3 is from lithiating LMO [20]. The separation into two peaks, 4 and 4.1 V, corresponds to a two-stage phase transition of one cubic spinel structure to another, a redistribution of Li^+ in the material at $Li_{0.5}Mn_2O_4$. For higher Li^+ content the cubic lattice continuously expands resulting in an additional peak [49, 50].

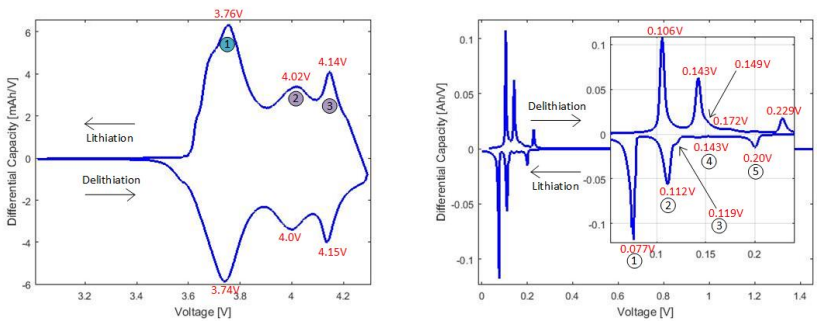

(a) (b)

Figure 3.7: ICA from C/10 constant current charge and discharge from lab scale cells made from material harvested from an commercial battery cell. (a) for the mixed cathode material, LMO and NMC, and (b) for natural graphite vs. Li-metal.

Commercial Cell ICA

A more detailed ICA was performed for one commercial cell by using an expanded RPT, including a C/10 charge and discharge cycle. Each peak correspond to a phase transition for one or both of the electrodes, figure 3.8.

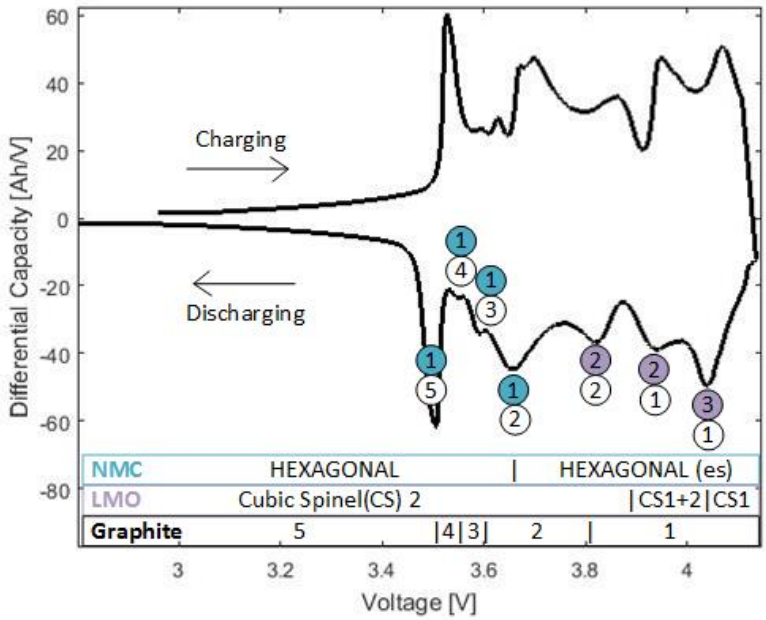

Figure 3.8: ICA for the fresh battery cell with the different materials stages indicated. Modified and drawn from [20, 32, 49].

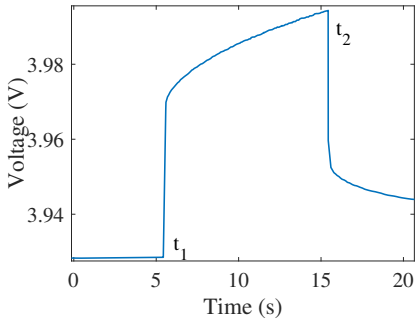

Figure 3.9: Voltage pulse response showing t_1 and t_2 used for the resistance calculations.

3.4.2 Resistance Characterization

The cell resistance is complex and highly depending on SOC, current, temperature, pulse duration and frequency. In aging tests several difference resistance measuring methods can be used to map the aging. In this project pulse resistance were chosen as tool. Two different pulses were used: 5C for 10s and 1C for 40s.

Pulse Resistance

The cell resistance during the aging tests were recorded by the RPT, see Section 3.3.1. The resistance is calculated by the voltage step method, based on Ohms law

$$R_{pulse} = \frac{u(t_1) - u(t_2)}{i(t_2) - i(t_1)} \tag{3.2}$$

where $u(t_1)$ is the voltage before the pulse and $u(t_2)$ the voltage at the end of the pulse, $i(t_2)$ and $i(t_1)$ are the currents at respective point, see figure 3.9.

The resistance has a strong temperature dependence. Figure 3.10a shows discharge resistance as a function of SOC measured at 26°C and 47°C. The resistance decreases with increased temperature, the 21°C degree increase gives rise to a 30% resistance decrease. The resistance in low SOC regions, less than 20% SOC, increases strongly while it in 20% to 60% SOC is almost constant. Between 60-70% SOC the resistance increases, then it decreases back to the same level as for 20-60% SOC.

The resistance is also depending on the current drawn from the battery and for how long time the current is drawn. In figure 3.10b the resistance for different current loads is shown. The current pulses were 10s long and 1h rest between the pulse, starting from 0.5A and up to 50A. The red dot is a

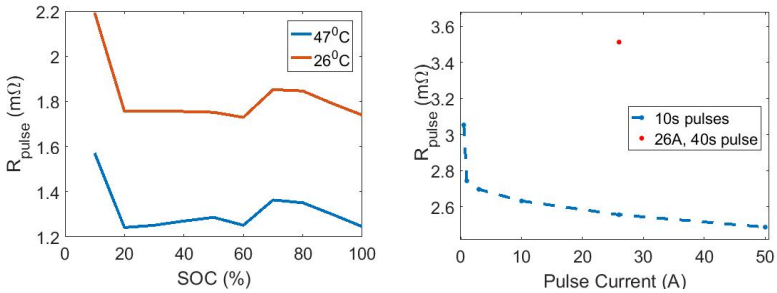

(a) (b)

Figure 3.10: Cell resistance dependence on current, SOC and temperature. (a) 10s 5C pulse discharge resistance as a function of SOC and T. (b) 10s pulse resistance at different current levels at 26°C, and the resistance for a 40s pulse at 1C.

the 26A 40s pulse performed in the RPT for the same cell performed before the tests with 10s pulses. The longer time a current pulse is drawn from the cell, the higher will the resulting resistance be.

Chapter 4

Battery Modeling

The aging mechanism that most of the physics-based models focus on is the capacity loss and resistance increase by the parasitic reactions occurring on the surface of the anode particles, the formation of an SEI layer. This is just one of many aging mechanisms, in the next section several other aging mechanisms are stated and their suitability to be modelled is brifely mentioned.

4.1 Aging Mechanisms and Simulation Challenges

In Table 4.1 some of the most important aging mechanisms in the battery are listed with the corresponding driving physical phenomena and the simulation ability of the aging mechanism stated. Several of the mechanisms that are applicable to be simulated might be highly difficult to incorporate in a model of a commercial cell, due to lack of material knowledge or material parameters. For most battery manufacturers the different additives and composition of the electrolyte is a trade secret.

Even with all the data given, the amount of reactions needed to be simulated is not fully applicable in a model. The choice of aging mechanisms has to be based on the cell investigated, what seems to be the main aging contributions. Another consideration is that a physics-based model requires several material parameters as input. This is another reason for the difficulty to simulate the aging mechanisms.

Table 4.1: Model applicability of different aging processes and possible detection method [8, 11, 15, 16, 19].

Aging Mechanism	Modeling	Physical phenomena	Consequences	Invasive detection	Non-Invasive detection
Loss of Li^+	applicable	SEI (and SPI) formation	Capacity retention and impedance increase	Post mortem analysis on aged cells	ICA peak intensity
Electrolyte decomposition SEI	applicable	SEI formation	Capacity retention and increased impedance on cycled cells.	Post mortem analysis on cycled cells.	ICA peak intensity
Electrolyte decomposition	applicable	Gas formation, dried out electrodes	Capacity retention, increased impedance and pressure and/or sudden death of cell.	Post mortem analysis on cycled cells.	Swelled cell
Additive degradation	partly applicable	Mainly to form stable initial SEI layer	impedance increase	Post mortem analysis	-
Binder degradation	partly applicable	Contact loss with active material/CC	impedance increase	Post mortem analysis	-
Loss of active material	applicable	Particles brake-down due to expansion/contraction, contact loss with CC, structural disorder	Capacity retention, Swelling of cell, impedance increase on cycled cells	Post mortem analysis	ICA peak shift
Cathode metal dissolution	applicable	Accelerates SEI formation	Capacity retention and impedance increase on cycled cells	Post mortem analysis	ICA peak intensity
Separator degradation	not applicable	Melts or corrodes	Short circuit of cell	Post mortem analysis	-
CC corrosion	applicable	Corrosion, loss of connection to active material	Capacity retention and increased impedance	Post mortem analysis	Impedance measurement

4.2 Electrochemical Model

The fundamentals of mathematically modelled electrochemical system were presented in Section 2.3. Here the model used in this thesis is described, in more detail. Some of the parameters used in the model are given in Table 3.1, 3.2 and 3.3.

4.2.1 Mass Transport in the Electrolyte

In the simulated system the electrolyte is assumed to be a binary electrolyte, consisting of a lithium salt dissolved in one solvent species. Letting + and − denote the ionic species, Li^+ and PF_6^-, the Maxwell-Stefan equation (see also (2.4)) for the binary electrolyte is used to account for the friction interaction between the species,

$$c_+ \frac{\partial \mu_+}{\partial x} = \sum_- \frac{RTc_+c_-}{c_T D_{+-}^{eff}} (\mathbf{v}_- - \mathbf{v}_+) \tag{4.1}$$

where c_T is the sum of all species concentrations. The effective diffusion coefficient, D_{+-}^{eff}, is calculated from the Maxwell-Stefan diffusivity of the pure electrolyte

$$D_{+-}^{eff} = D_{+-}\epsilon^\beta \tag{4.2}$$

where ϵ is the electrolyte volume fraction and β the Bruggeman coefficient [51]. All the effective parameters used in the porous structures in this model uses this correlation.

From now on D will be used for the efficient diffusion coefficient if nothing else is stated. Writing (2.2) for the two component electrolyte, solvent and salt, gives

$$N_+ = \frac{c_T c_+}{c_-} D_+ \nabla ln a_+ - \frac{z_+ F}{RT} \frac{c_T c_+}{c_-} D_+ \nabla \phi + c_+ v_- \tag{4.3}$$

where a_+ is the activity ($\nabla \mu_+ = RT \nabla ln a_+$) [36] and the total concentration calculated from the salt concentration, $c_l = c_{+/-}$, and solvent concentration, c_{solv}, assuming electroneutrality.

$$c_T = 2c_l + c_{solv} \tag{4.4}$$

The solvent concentration is calculated from the partial molar volume V_m of the salt and solvent

$$c_{solv} = \frac{1 - V_m^l}{V_m^{solv}} \tag{4.5}$$

Combining (4.3) and (2.3) while taking into account the porosity, the material balance for the salt becomes

$$\epsilon_l \frac{\partial c_l}{\partial t} = \nabla \left[(1 - c_l V_m^l) \left(\left(1 + \frac{\partial ln f_\pm}{\partial ln c_l} \right) \frac{c_T}{c_{solv}} \epsilon_l^\beta D_l \nabla c_l + \frac{i_l (1 - t_+)}{F} \right) \right] \quad (4.6)$$

where the electrolyte current density is expressed by

$$i_l = \kappa_{eff} \left(-\nabla \phi_l + \frac{2RT}{c_l F} \left(1 + \frac{\partial ln f_\pm}{\partial ln c_l} \right) (1 - t_+) \nabla c_l \right) \quad (4.7)$$

where $f_\pm$ is the salt activity coefficient and κ_{eff} electrolyte conductivity [40, 51].

4.2.2 Potential and Current Coupling

The potential, in the current collectors and the porous electrode materials are calculated by Ohms law from the applied current density

$$\mathbf{i}_s = -\sigma_s \nabla \phi_s \quad (4.8)$$

where σ is the conductivity. In the porous material, the effective conductivity

$$\sigma^{eff} = \epsilon^{\beta_s} \sigma, \quad (4.9)$$

is used. The copper current collector, on the anode side, is connected to ground, $\phi = 0$V, and the aluminum, on the cathode side, to the current feed, $-\mathbf{n} \cdot \mathbf{i} = i_{applied}$. To couple the active material and electrolyte, a balance over the volumetric current is used

$$\nabla \cdot \mathbf{i}_l = i_{v,tot} = \sum_m i_{v,m} (+ i_{v,dl,add}) \quad (4.10)$$

$$\nabla \cdot \mathbf{i}_s = -i_{v,tot} \quad (4.11)$$

The volumetric current in each mesh node, $i_{v,m}$, is the sum of the Faradaic current density (j_F), the current density from electrochemical reactions, and the charging of double layers on the surface of the active material particles (j_{dl}),

$$i_{v,m} = S_a i_{loc} = S_a (i_F + i_{dl}) \quad (4.12)$$

where S_a is the active specific surface area of the electrode material. The particles are assumed to be spherical, giving the following expression for the active specific surface area

$$S_a = \frac{3\epsilon_s}{r_p} \quad (4.13)$$

where r_p is the particle radius [13, 40].

4.2.3 Electrochemical Reactions

The electrochemical reactions are considered to be of intercalation and deintercalation type and occur on the surface of the active electrode particles. During the intercalation, Li^+ enters into the material, is reduced and during deintercalation, is oxidized back to Li^+, which exits the material. The reaction kinetics is assumed to follow the Butler-Volmer (B-V) equation

$$i_F = i_0 \left(exp\left(\frac{\alpha_a F \eta}{RT}\right) - exp\left(\frac{-\alpha_c F \eta}{RT}\right)\right) \tag{4.14}$$

with

$$i_0 = F(k_c)^{\alpha_a}(k_a)^{\alpha_c}(c_{s,max} - c_s)^{\alpha_a}(c_s)^{\alpha_c}\left(\frac{c_l}{c_{l,ref}}\right)^{\alpha_a} \tag{4.15}$$

and

$$\eta = \phi_s - \phi_l - E_{eq}(c_s, T) - \Delta\phi_{s,film} \tag{4.16}$$

where η is the overpotential, E_{eq} the equilibrium potential of electrode material, α the reaction rate coefficient, and $\Delta\phi_{s,film}$ is the potential difference from the resistive film that always is formed on the graphite particles (SEI) and to a smaller extent on the cathode particles (SPI).

$$\Delta\phi_{s,film} = i_{tot} R_{film} \tag{4.17}$$

where R_{film} is the film resistance [13].

4.2.4 Double Layer Capacitance

The double layer capacitance, $C_{dl,i}$, is assumed to arise between the electrolyte and all surfaces in the electrode components. The double layer is assumed to be charged by Li^+ and the current densities are calculated from

$$i_{dl,S} = C_{dl,S}\frac{\partial(\phi_s - \phi_l - \Delta\phi_{s,film})}{\partial t} \tag{4.18a}$$

$$i_{dl,addS} = C_{dl,addS}\frac{\partial(\phi_{adds} - \phi_l)}{\partial t} \tag{4.18b}$$

$$i_{dl,cc} = C_{dl,cc}\frac{\partial(\phi_{cc} - \phi_l)}{\partial t} \tag{4.18c}$$

where (4.18a) is the contribution from the active material, (4.18b) from the conductive additives and (4.18c) from the current collectors [40]. The double layer capacitance affects the results when simulating dynamic behavior, due to uncertainty in parameters for (4.18c) and (4.18b) only $i_{dl,S}$ is added to the model so far.

4.2.5 Mass Transport in the Electrode Materials

The particles are assumed to be spherical and to account for the concentration in the active material, a pseudo dimension is added to the model. The transport of Li^+ in the particles is assumed to occur through diffusion, which is modelled by Fick's second law [51]

$$\frac{\partial c_s}{\partial t} = \frac{D_s}{r^2}\frac{\partial}{\partial r}\left(\frac{r^2 \partial c_s}{\partial r}\right) \tag{4.19}$$

with the boundary conditions

$$\frac{\partial c_s}{\partial r}|_{r=0} = 0 \tag{4.20}$$

$$-D_s \frac{\partial c_s}{\partial r}|_{r=r_p} = \sum_m \frac{i_{loc,m}}{F} \tag{4.21}$$

4.2.6 Aging Through SEI Growth

The SEI growth originate from decomposition reactions of the solvent at the graphite surface [52, 53]. The solvent consists of EC, DMC, EMC, and additives. The concentration of the different solvents is unknown and for this model only decomposition reactions of EC are considered. The main products are considered to be dilithium ethylene dicarbonate ($(LiOCO_2CH_2)_2$) [52,54] and lithium carbonate (Li_2CO_3) [52,55]. The reaction considered is reduction of EC to $(LiOCO_2CH_2)_2$ and further decomposition [56] or electrochemical reduction [57] of $(LiOCO_2CH_2)_2$ according to [58]:

$$2(CH_2O)_2CO + 2e^- + 2Li^+ \rightarrow (LiOCO_2CH_2)_2 + C_2H_4 \tag{4.22a}$$

$$(LiOCO_2CH_2)_2 \rightarrow Li_2CO_3 + C_2H_4 + CO_2 + 1/2O_2 \tag{4.22b}$$

$$(LiOCO_2CH_2)_2 + 2Li^+ + 2e^- \rightarrow 2Li_2CO_3 + C_2H_4 \tag{4.22c}$$

The end product of reactions (4.22b) and (4.22c) are containing Li_2CO_3, which in this model, therefore is considered the final product. The SEI is assumed to grow only during charging and the decomposition reaction triggered by the overpotential

$$\eta = \phi_s - \phi_l - \Delta\phi_{s,SEI} - E_{eq,SEI} \tag{4.23}$$

where $E_{eq,SEI} = 0.4$ V vs Li/Li^+ [8]. The SEI growth introduces an increasing resistance proportional to the thickness of the SEI layer, d_{SEI},

$$R_{SEI} = \frac{d_{SEI} + \Delta d_{SEI}}{\kappa_{SEI}} \tag{4.24}$$

where κ_{SEI} is the conductivity of the SEI layer. The thickness is determined by the accumulated amount of Li^+ lost due to side reactions

$$\Delta d_{SEI} = \frac{Q_{SEI} M_{SEI}}{2 Sa_{anode} \rho F} \tag{4.25}$$

where M_{SEI} is the average molar mass of the products formed in the SEI and ρ the density of Li_2CO_3. Q_{SEI} (C/m^2) is the irreversibly capacity loss to the side reactions directly proportional to the concentration, c_{SEI}, of Li^+ bound in the SEI layer

$$Q_{SEI} = c_{SEI} F \tag{4.26}$$

The concentration accumulated in the SEI layer is calculated from

$$\frac{dc_{SEI}}{dt} = \frac{-i_{SEI} Sa_{anode}}{F} \tag{4.27}$$

where the current from the SEI reactions is assumed to follow B-V kinetics with concentration dependence

$$i_{kin,SEI} = i_{0,SEI} \left(\frac{c_p}{c_{p,ref}} exp\left(\frac{\alpha_a F \eta}{RT} \right) - \frac{c_+}{c_{+,ref}} \frac{c_l}{c_{l,ref}} exp\left(\frac{-\alpha_c F \eta}{RT} \right) \right) \tag{4.28}$$

where p stands for the product produced in the side reaction. The equation was simplified to a cathodic Tafel approximation by assuming irreversible (only cathodic) reaction, thus, dropping the first term of (4.28) [8]

$$i_{kin,SEI} = -i_{0,SEI} \frac{c_+}{c_{+,ref}} \frac{c_l}{c_{l,ref}} exp\left(\frac{-\alpha_c F \eta}{RT} \right) \tag{4.29}$$

The exchange current density $i_{0,SEI}$ was first taken from [8] and later estimated from simulations to tune the aging so that the thickness of the SEI layer would be in the order of 300 nm, reported by [30], at EOL for a simulated cell in the full SOC range.

As the SEI layer grows the side reactions are assumed to become mass transport limited and a limiting current in accordance to the Nernst boundary layer was used

$$i_{lim} = -\frac{c_l D_{l,sei} F}{d_{SEI}} \tag{4.30}$$

where c_l is the solvents bulk concentration, $D_{l,sei}$ the diffusion coefficient for the SEI layer and c_l the bulk concentration in the electrolyte. The relation for first order mass transport limitations was used

$$i_{SEI} = \frac{i_{kin,SEI}}{1 + \frac{i_{kin,SEI}}{i_{lim}}} \tag{4.31}$$

Porosity Change due to SEI Growth

With an increasing SEI layer the volume balance in the electrode needs to be adjusted. The amount of active material is kept constant while the increase in SEI layer is reducing the volume fraction of electrolyte in the porous structure. This is a rough estimation, since the SEI layer is likely to reduce the porosity of the active material and will not grow evenly on all surfaces. It might also isolate parts of the active material from the current collector. These effects have so far been neglected.

The electrolyte volume fraction is decreased according to:

$$\epsilon_l = 1 - \epsilon_s - \epsilon_{add} - \epsilon_{SEI} \tag{4.32}$$

where ϵ_s and ϵ_{add} are constant.

$$\epsilon_{SEI} = V_{SEI}/V_{tot} = d_{SEI} S_a \tag{4.33}$$

4.3 Model Validation

In this section the calibration of the model and estimation of model parameters are presented. Experimental data from RPT and half cell measurements were used to fit parameters and to calibrate the model to the lifetime tested cells.

4.3.1 Parameter Estimation

Resistance Estimation

Current pulses were simulated in the model and the voltage response compared to to measured pulse data, the RPT test. The simulation showed larger voltage response than expected and the ohmic resistance was estimated by calculating the pure resistive contribution from all parts in the electrochemical cell, Table 4.2. From this estimation the IR contribution for different currents were calculated. The results showed that the additional resistance was not coming from the material's resistivities. The high resistivity was contributed to the reaction rates for the two materials and these were adjusted to give the same voltage increase as the measured data, figure 4.1a.

Diffusion Coefficient Estimation

The diffusion coefficient as a function of potential for graphite was taken from [38] and for NMC as a function of SOC from [59]. Since the cathode is a mixture of NMC and LMO, the diffusion coefficient for the cathode side

Table 4.2: The estimated pure resistive contribution in Ω from the different components in the cell.

R_{tot}	R_{Al}	$R_{s,pos}$	$R_{l,pos}$	R_{sep}	$R_{l,neg}$	$R_{s,neg}$	R_{Cu}
1.2e-3	2.62e-13	2.44e-06	6.18e-04	2.84e-04	2.64e-04	2.12e-06	1.55e-13

was fitted to RPT data from a fresh cell, figure 4.1a. The difference in the simulated and experimental pulse responses is contributed to the corresponding difference in the OCV, figure 4.1b. Further the model only consists of one material for the cathode side, with parameters measured or calculated to simulated the mixed cathode material. To get a better fit, the model should for prediction of dynamic current-voltage studies be simulated with two separate materials. For the aging model, however, this fit is considered sufficient.

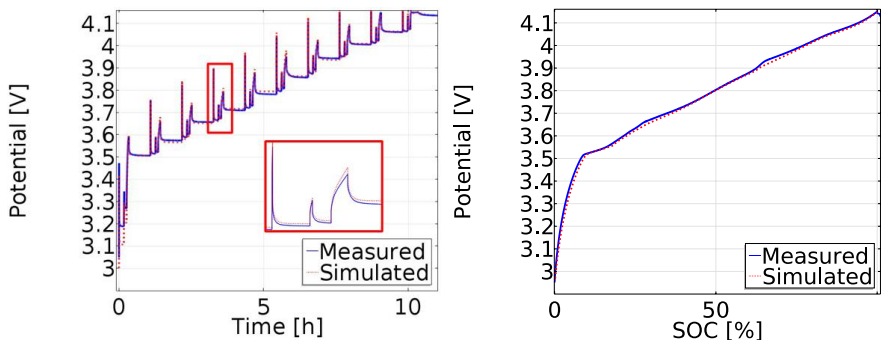

(a) (b)

Figure 4.1: (a) Simulated RPT charge pulses (red, dotted) compared to measured RPT charge pulses (blue, solid) on a fresh cell in 25°C. (b) Pseudo OCV from C/10 charge data compared to simulated results.

4.3.2 Calibration using Experimental data

Experimental data were used to visualize the difference to the physics-based model using ICA. The agreement between the simulation and measurements is better at 0.1C than for 1C. For the 1C data four peaks instead of the expected three peaks are seen, figure 4.2. In the measurement data the last and first data points in the charge/discharge had to be removed in the processing and therefore only data up to 4.11V is shown. The beginning of the fourth peak can be seen around 4.1V. There is also a stronger polarization in the simulation compared to the experimental data at 3.6 V but lower at

the end of the charge, around 4 V. This could be an effect of not including a resistive film on the cathode side in combination of the fitted diffusion coefficient.

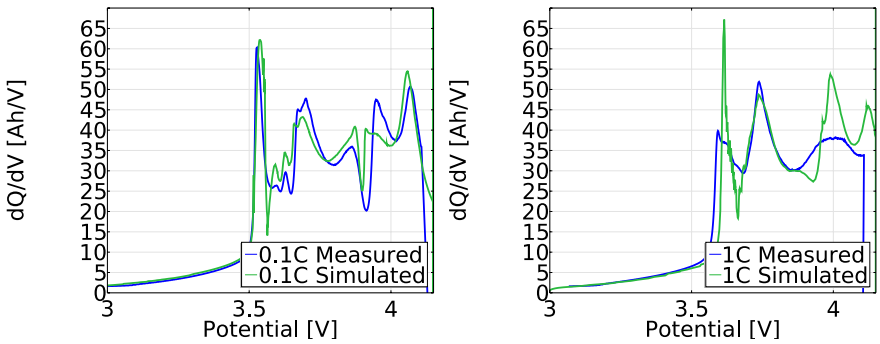

(a) (b)

Figure 4.2: ICA performed for two different current rates, (a) 0.1C and (b) 1C, comparing simulated data with measured data of a fresh cell charge at 25°C.

4.3.3 Active Material Loss

The model was used to separate two different aging phenomena, loss of anode and cathode materials as a step in analyzing the result from the lifetime testing. As the experimentally measured ICA was performed with 1C, the simulation was performed in this way as well. Important to note is that all the following data were performed without any film resistance.

The results from the simulations of loss of anode and cathode material in different combinations are shown in figure 4.3. The peaks are numbered from left to right, 1 to 4.

Loss of anode material, figure 4.3a, shows a clear shift of peak 1 and 2 towards lower potentials, increasing with anode loss. Peak 4 disappears after 20% anode loss and the amplitude of peak 2 and 3 increases. Loss of cathode material strongly influences the amplitude of all peaks, especially peak 2, and shifts peak 3 and 4 towards lower potentials.

Simulating a main loss of anode material, 20%, and a smaller loss of cathode material, 10%, figure 4.3c shows small amplitude changes and a shift of all peaks towards lower potentials. A smaller new peak between peak 2 and 3 can also be seen. This additional peak is also observed in figure 4.3a.

The opposite case, figure 4.3d, with a dominating cathode loss, shows that

except for the overall amplitude loss, the changes in position in peak 1 and 2 are small. Peak 3 and 4 shift more to lower potentials and Peak 3 splits into tow peaks, a tendency to this can also be seen in 10% cathode loss.

Simulating 20% loss in both electrodes, figure 4.3e, results in lower peak amplitude, but higher than the case of 20% cathode and 10% anode loss. All peaks are shifted to lower potentials.

To summarize, although this theoretically constructed material loss is not fully representative for the aging in a battery cell, this gives valid information in what to expect from the different aging mechanisms. Cathode loss affects the capacity to a grater extent than anode loss, and the anode loss induces larger shift in the peak positions.

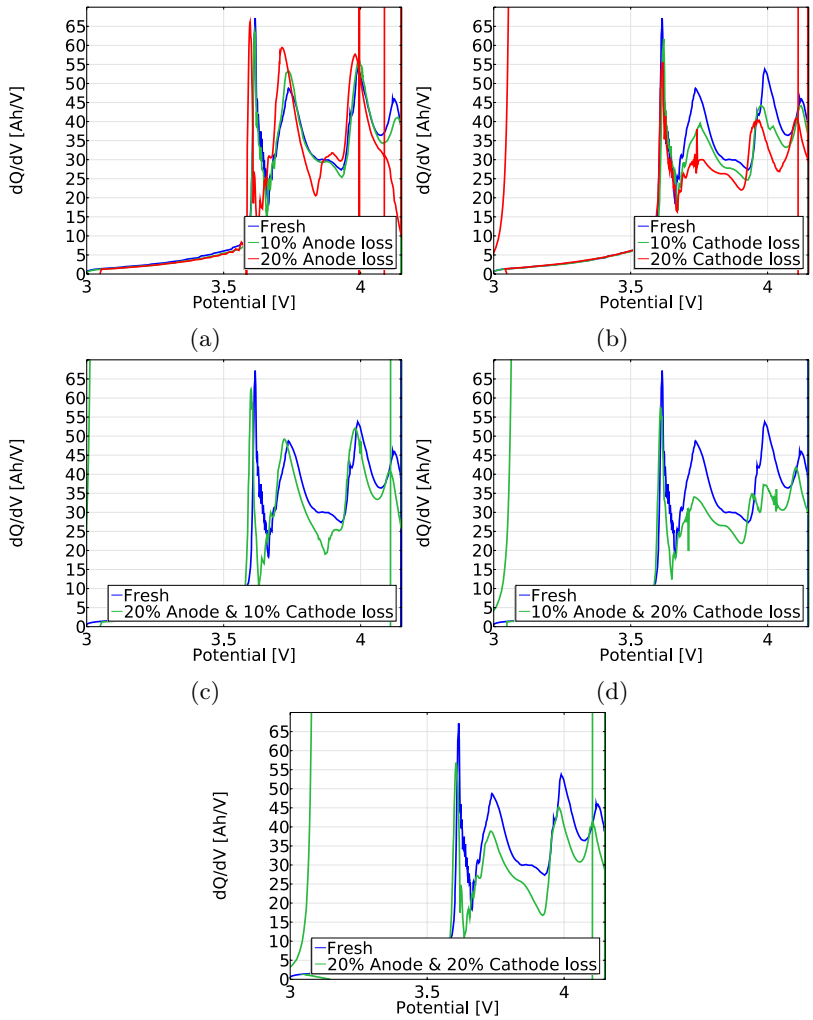

Figure 4.3: ICA from simulations showing how the peaks shift with different combinations of loss of active material. First only one-sided material loss is simulated (a) anode loss and (b) cathode loss. Secondly in three different combinations; (c) 20% anode loss and 10% cathode loss, (d) 10% anode loss and 20% cathode loss, and (e) 20% loss of both materials. The peaks are numbered from left to right, 1 to 4.

4.4 Aging Simulation Results

The aging in this model is a result from SEI layer growth, from side reactions on the anode/electrolyte interface. The growth of the SEI results in three different contributions, consumption of cyclable Li^+, increased film resistance on the anode, and decreased volume fraction of the electrolyte. The aging parameters for the SEI reaction were fitted to the capacity loss for the +2C/-2C 0-90% SOC interval in 25°C, figure 4.4.

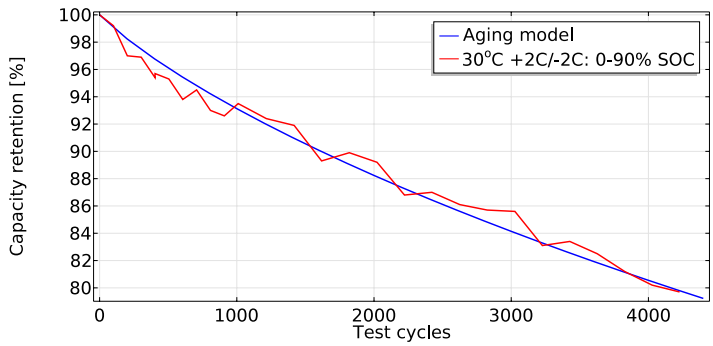

Figure 4.4: Simulated capacity retention, blue line, the aging parameters were fitted to represent the aging of +2C/-2C 0-90% SOC at 25°C, red line.

4.4.1 Consequences of SEI Build up

The capacity retention due to SEI build up is overestimated in the model, since it is the only aging mechanism included all loss has to come from this. Therefore, the simulated SEI thickness is considered to be larger than in the actual cell. Postmortem analysis will hopefully show how thick the layer is. The expected thickness is in the rage 3-300 nm based on literature [30, 35].

The thickness of the SEI is depending on the current in each segment of the anode, figure 4.5a. During charging the current is highest close to the separator (sep), at 64.5 μm, and this can be seen in the distribution of the thickness, it is largest at the sep and thinnest at the cc, 0. Therefore, the volume fractions are presented for both the cc and sep.

The loss of electrolyte contributes to a small resistance increase in the model, although the main resistance increase is from the SEI layer, figure 4.5b and 4.6a. The lost electrolyte volume is filled with SEI, figure 4.6b.

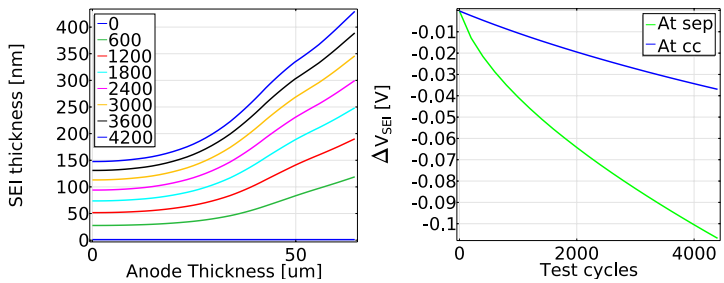

(a) (b)

Figure 4.5: Simulated +2C/-2C cycling in 0-90% SOC at 25°C (a) SEI growth and (b) the resulting voltage drop over the SEI film for 1C.

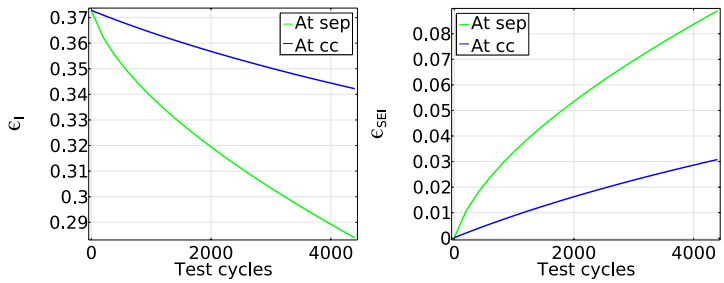

(a) (b)

Figure 4.6: Simulated change of volume fraction for (a) the electrolyte, ϵl, and (b) the SEI, ϵl, for +2C/-2C cycles in 0-90% SOC at 25°C.

4.4.2 Contribution of Aging Mechanisms

In the simulated ICA, peak 1 loses amplitude as the SEI grows, figure 4.7. The peaks changes there appearance as well as slight shifts towards the left, except for the last peak at EOL that is moved tp the right. The growth rate is faster in the beginning and slows down as the thickness increases. From this, the main contribution from the SEI is the reduction in amplitude in peak 1.

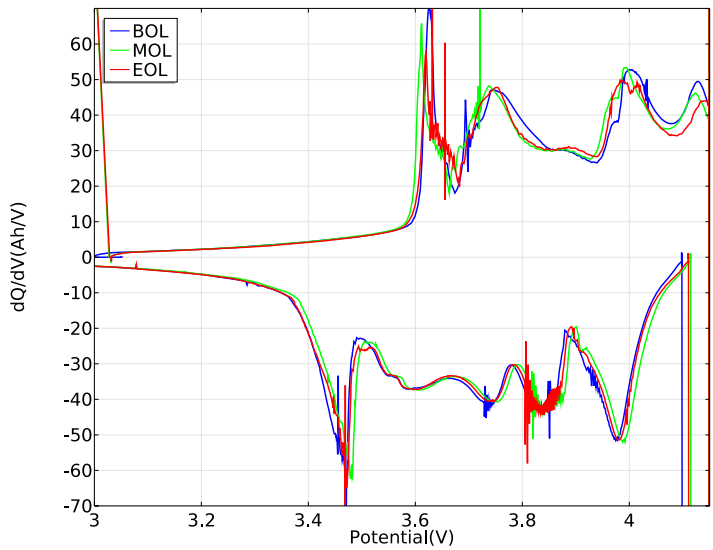

Figure 4.7: Simulated ICA for +2C/-2C 0-90% SOC at 25°C for BOL, MOL and EOL.

Chapter 5

Battery Aging

The results from the cycle and calendar aging tests are presented in this chapter. The effect of several different parameters, such as temperature, C-rate, SOC level and DOD, has been investigated. All cycling data are recalculated and presented as FCE for a straight forward comparison of test results.

5.1 Lifetime Aging Tests

The lifetime cycling was performed in four different DOD, 10%, 60%, 80% and 90%. For the targeted application, a 100% DOD is not under consideration and has, therefore, not been included in the test matrix. The focus has been on studying the effects of different SOC levels and C-rates, where charge rates and discharge rates are noted with +XC respectively -XC.

For cells cycled during long time periods two data points can be seen for the same cycle number, this indicates that the cell has been in room temperature for 1 month during vacation time, one RPT before and one after the vacation period. The resistance displayed in this chapter is the 50% SOC 10s 5C discharge resistance. The given temperatures in the figures are the average cycling temperatures. The various test protocols give rise to different temperature increases, the resulting cell temperatures are therefore not the same as the climate chambers temperature.

As the temperature is an important factor in the aging process, calendar aging at 25, 35 and 45°C and at 15, 75 and 90% SOC were performed. A total of 18 cells were tested, including replicas.

5.2 Temperature Dependence

High temperature decreases the lifetime of the battery during both cycling and calendar aging in accordance with published literature [4, 5, 9, 10, 20, 23].

5.2.1 Calendar Aging

The result from the calendar aging, figure 5.1, is in coherence with previous published literature [5, 9]. Interesting to note is that in 25°C there is no difference between the capacity retention in the two high SOC levels. However, a higher increase in the resistance can be seen for the 90% SOC level. This is coherent for all temperatures, the higher SOC results in higher resistance. Important to observe is that the resistance increase is very small in 25 and 35°C, only in 45°C clear resistance increase can be seen.

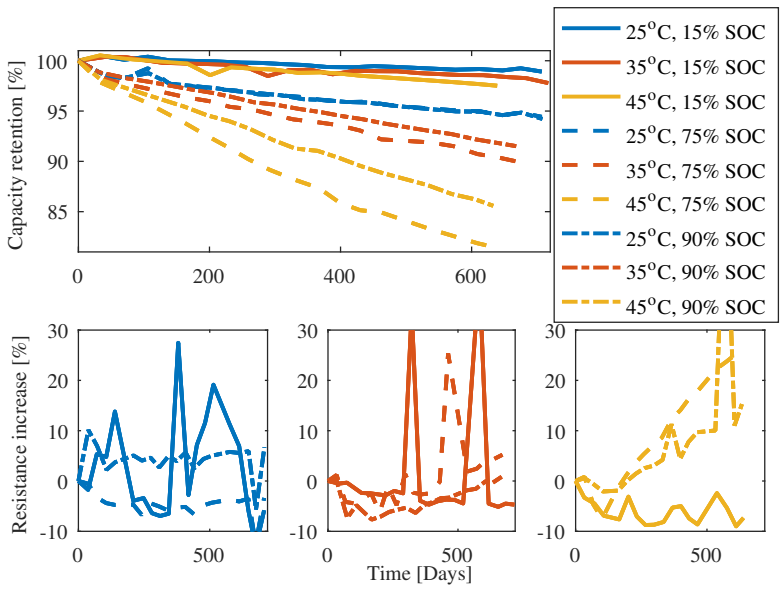

Figure 5.1: Calendar data for 25, 35 and 45°C and 15, 75 and 90% SOC.

5.2.2 Cycling Aging

Lifetime cycle tests performed in 0-90% SOC with +2C/-2C, show clear difference in cycle life for increasing temperature, figure 5.2. The higher resistance at increasing temperature, and its proportionality to the capacity loss, suggests that the higher temperatures triggers more SEI reactions that causes the faster decay in capacity. The results definitely confirms the stat of the art assumptions regarding aging and temperature.

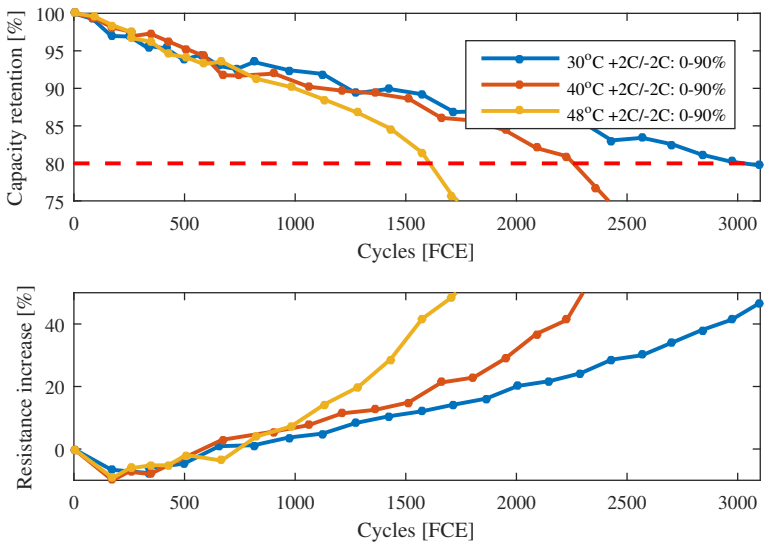

Figure 5.2: The effect of ambient temperature on aging at 25, 35 and 45°C for test performed in +2C/-2C in 0-90% SOC. The cells average cycling temperature is indicated in the legend.

The temperature effect is less visible with +2C/-2C cycling in 10% SOC intervals, figure 5.3. In the low SOC regime the 25 and 45°C temperatures seem to have equal aging, while the test run in 35°C shows slightly less aging, see figure 5.3a. The resistance increases proportionally with the capacity loss as for the 90% DOD, although the resistance increase is lower. It is first for 60-70% SOC that a clear temperature dependence can be seen. The resistance increase and capacity loss is faster at 45°C, reaching the same EOL resistance increase as the 0-90% SOC.

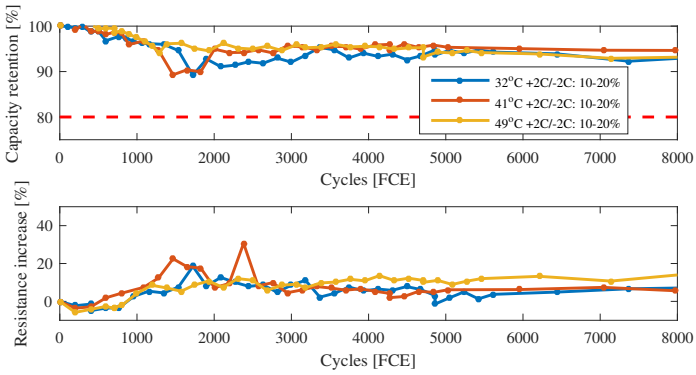

(a)

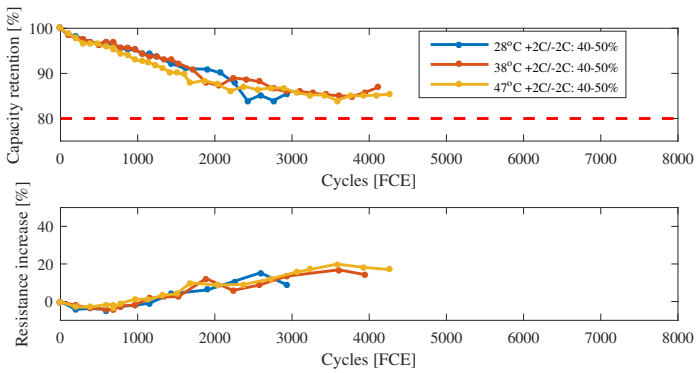

(b)

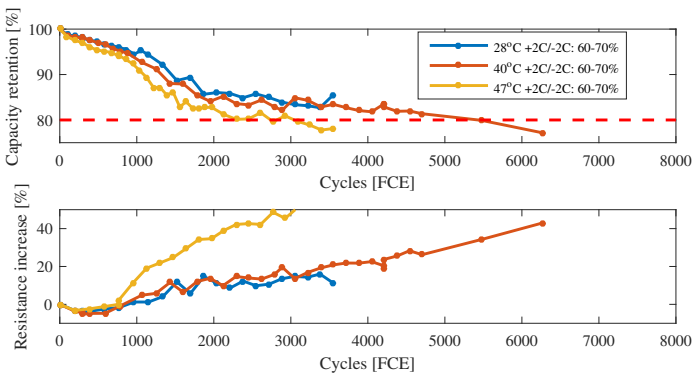

(c)

Figure 5.3: Symmetric +2C/-2C tests performed in 10% DOD at (a) 25, (b) 35 and (c) 45°C ambient temperature.

5.2.3 Current Rate

To see the effect of different current rates, C-rates, two test series were performed at 40°C temperature. One asymmetric test series with a 1C charge with either 1C, 2C, or 3C discharge. The second series with symmetric charge and discharge tests with 1C, 2C, 3C, and 4C. In addition to these series, an asymmetric test with 3C charge and 1C discharge was performed to study the effect of fast charging.

The results for increasing discharge rate with a 1C charge, figure 5.4, shows that increasing discharge rate increase the aging, as expected [10, 47]. The reversed asymmetric cycle, +3C/-1C does not follow the same behavior, indicating that the fast charging triggers different aging mechanisms, see Section 5.4. The resistance has only increased with 19% at EOL, compared to the 32% for the +1C/-3C.

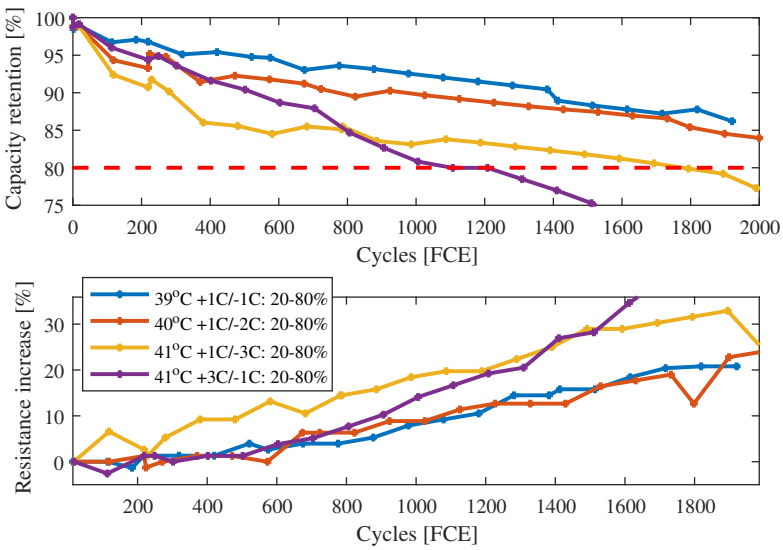

Figure 5.4: Asymmetric test patterns performed in 20-80% SOC in 40°C ambient temperature for different C-rates.

For the symmetrical cycles, the aging increases with higher C-rate, figure 5.5. What was not expected is the large capacity drop during the initial cycles for the higher C-rates. This has been seen in previous studies in 10% DOD [5], although in larger DOD the capacity loss is expected to be accelerated as the cycling proceeds [4, 47].

The initial drop in capacity during the first 100 FCE is larger for the

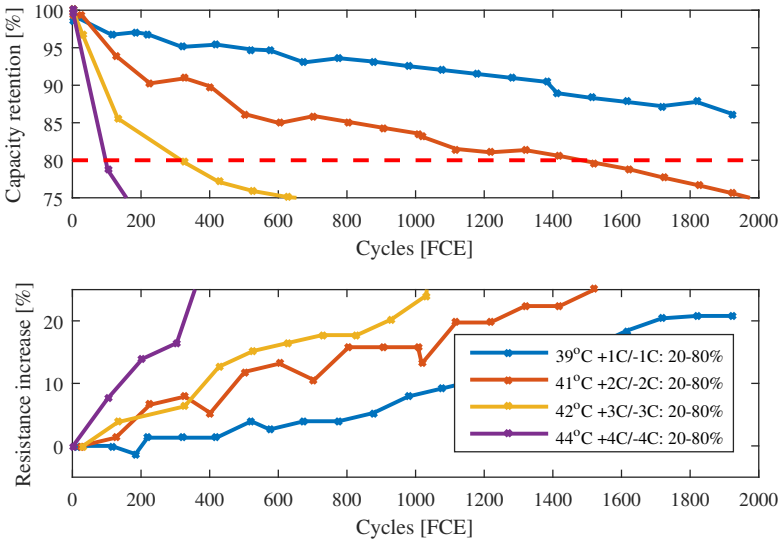

Figure 5.5: Symmetric test patterns performed in 20-80% SOC in 40°C ambient temperature for different C-rates.

higher C-rates compared to 1C charging. The aging is then reduced to a linear behavior, although faster for higher C-rates. The tested cells are more energy than power optimized and are not designed to handle higher than 3C CC discharge. This is also clearly seen in the data, the aging in 4C was more severe than expected and the cell dropped below the end of life (EOL) criteria before the second RPT could be performed.

Effect of C-rate and SOC Level

To understand in which SOC level high current is most detrimental, three symmetric C-rate tests were performed in two different 10% SOC intervals. The SOC intervals were chosen so that 4C could be run without risk of reaching the voltage limits during cycling.

In the low SOC interval, 10-20% SOC, increased C-rate give rise to a larger initial capacity drop, figure 5.6a. The capacity is then recovered and for the lower C-rates this recovery is more pronounced. The loss in capacity after the initial cycles is more or less constant. What causes the initial capacity drop and recovery is not known and further studies need to be performed to answer this. However a hypothesis is that active material gets blocked during film formation on the surfaces and in pores, mainly on the anode side.

This can be a result of local SEI formation causing lower porosity or clogging of pores. Later this material is unblocked as the SEI layer is reformed or reversed.

In the higher SOC regime, 60-70%, there is a clear difference between 1C and higher C-rates, SOC figure 5.6b. The difference between 2C and 4C is smaller, the test in 4C reaches EOL after 4130 FCE and 2C after 5470 FCE. Here it can also be seen that the initial capacity drop is larger for higher C-rates. In this SOC interval, a capacity recovery after the drop can not be seen.

5.2.4 Drive Cycle vs. Constant Current

The difference in aging between using a CC and a dynamic drive cycle, Hyzem Rural, was determined for two different temperatures. The cells were cycled in 10-90% SOC with 1C charge rate and 2C discharge rate. The Hyzem Rural drive cycle was scaled so that the RMS current was 2C. Important to note is that the Hyzem Rural cycle takes longer time, 111 min, compared to the CC 2C cycle, 87 min, due to stop times included in the cycle, figure 3.5.

The expected effect of temperature is obvious from the double lifetime of the cells cycled in 25°C compared to 45°C. The difference in aging between the two test regimes seems to be reduced as the temperature increase.

Investigating the effect of current load shows that the CC results in a stronger aging compared to the Hyzem cycle, figure 5.7. The cause for this could be that in the Hyzem cycle the cell is not under constant strain, instead it is allowed to relax during the stop times. The results indicates that it would be valuable to expand the test matrix with an additional test including stop times also in the CC cycle. This to achieve higher similarities between the two test regimes and to further understand whether dynamic cycles induces the same stress as synthetic CC cycles.

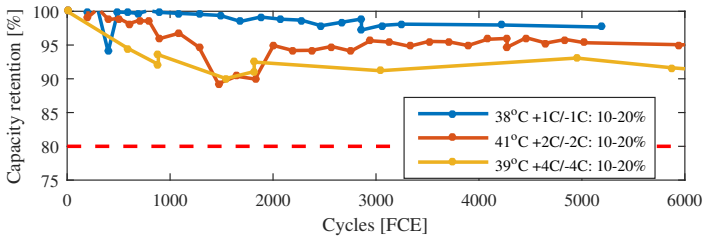

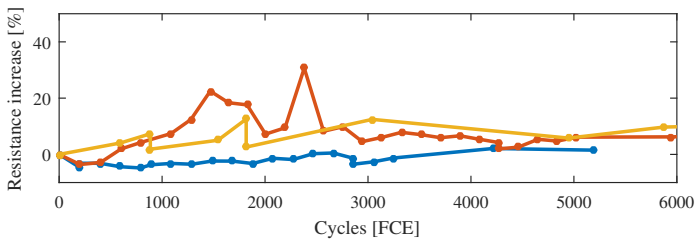

(a)

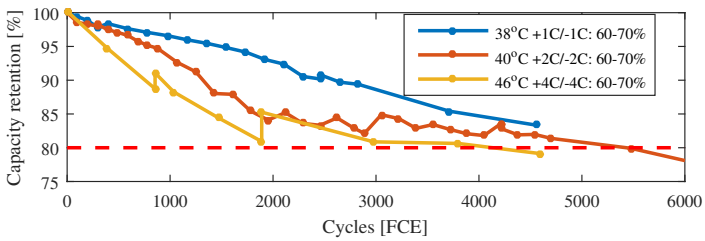

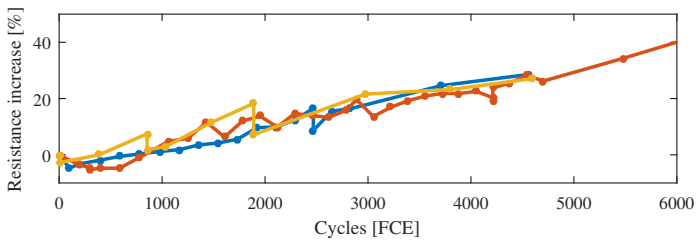

(b)

Figure 5.6: Symmetric tests performed in 10% DOD at 35°C with symmetric charge and discharge currents +XC/-XC, (a) in 10-20% SOC and (b) in 60-70% SOC.

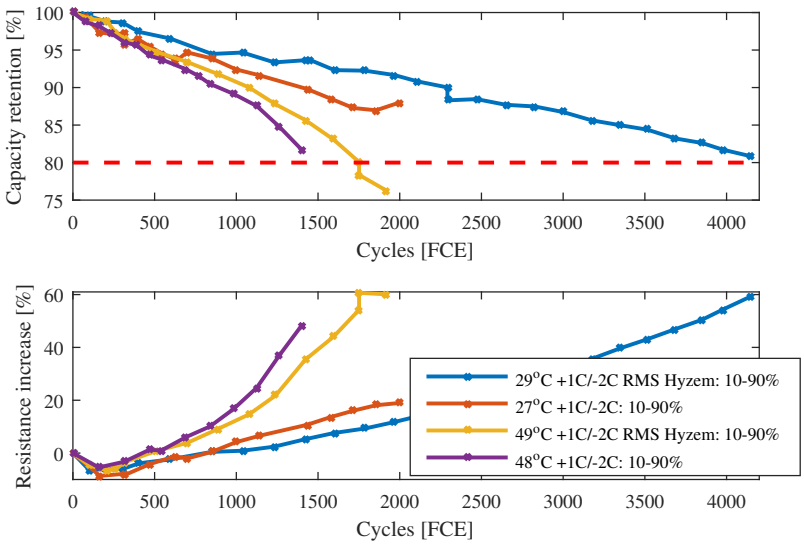

Figure 5.7: Comparison of CC discharge, without stop time, and dynamic drive cycle pattern, including stop time, as a function of FCE at 25 and 45°C.

5.3 Aging Dependence of SOC

When establishing the SOC window for an application there are several parameters to be considered, DOD, SOC interval placement, and application requirements. As was seen from the calendar aging, the SOC level has a strong correlation to the aging of the cell.

5.3.1 Aging in Small SOC Intervals

To understand in what SOC level the aging is most severe during cycling, tests in different 10% SOC intervals were performed at three temperatures; 25, 35 and 45°C. All SOC intervals in Table 3.4 were not included for all temperatures, however, the selection presented is assumed to cover the important findings.

There is a clear separation between the results originating from the low and high SOC intervals, figure 5.8. In the higher SOC intervals a more rapid aging can be observed compared to the lower SOC intervals. The previously described behavior with an initial capacity drop followed by a capacity recovery is clearly seen for the low SOC intervals. As previously stated, the hypothesis is that reformation of the SEI or reversible SEI reactions take place and anode material previously blocked by SEI layer is unblocked.

After the recovery, the cells are stabilizing on a capacity level above 90%, at 35°C even above 95%. What causes the stability in capacity over such extended number of cycles is not yet understood, and will be addressed by further studies including postmortem analysis. The hypothesis is that the SEI formed is very stable, the small SOC interval give rise only to small anode material expansions, which leaves the SEI intact, or with very few cracks. Therefore, the additional SEI formed, which is the main source for capacity loss, is limited. The resistance increase follows the coherent pattern proportional to the capacity loss but is not explicitly shown here, see figure 5.3 for the resistance of nine of the cells.

High SOC has been proven to increase side reactions forming SEI layer on the anode side [8, 31]. This is also seen in the aging patterns, where high SOC shows more rapid aging. Above 60% SOC no large differences in aging can be seen while 40-50% SOC shows slightly less aging. For the low SOC intervals only very moderate aging is observed.

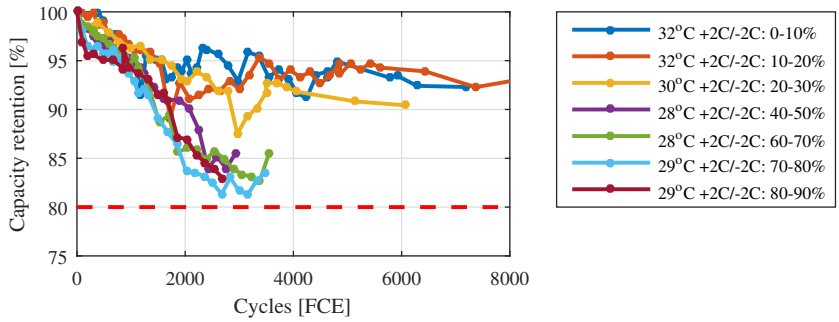

(a)

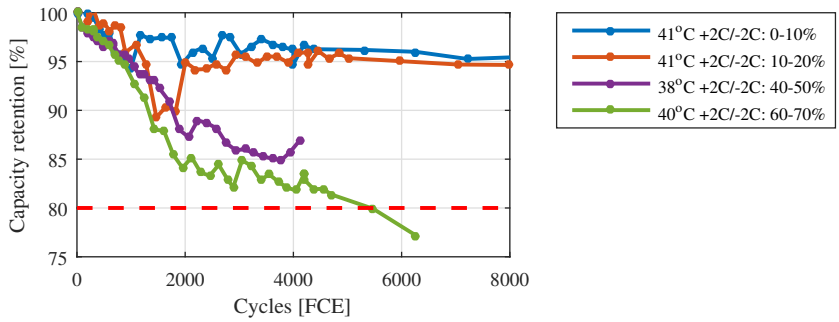

(b)

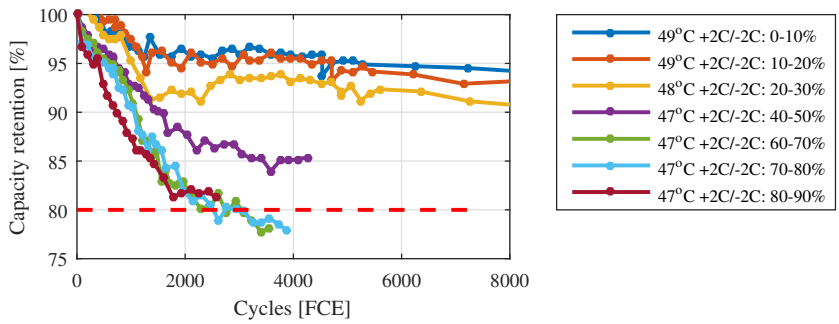

(c)

Figure 5.8: Symmetric +2C/-2C tests performed in 10% DOD at (a) 25, (b) 35, and (c) 45°C.

5.3.2 Effect of high SOC

High SOC is clearly damaging to the cells and to study this in more detail a test was setup to investigate how a cell age while using CC-CV charge, limiting the voltage to 90% SOC level (4.056 V). The previously presented test in the 80-90% SOC interval, figure 5.8, used CC charging without limiting the voltage and the cell voltage was allowed to increase above the 100% SOC limit (4.15 V). As the resistance increased, so did the charge voltage. Due to safety considerations the CC charging lifetime test was stopped when the charge voltage increased to 4.24 V. This unfortunately occurred before the EOL criteria was reached.

As expected, the higher voltage increases the aging, but not dramatically, figure 5.9. The average voltage for the cells during cycling were similar, even slightly higher for the CC-CV cell. This indicates that the increased aging is related to the higher cut-off voltage for the CC cell.

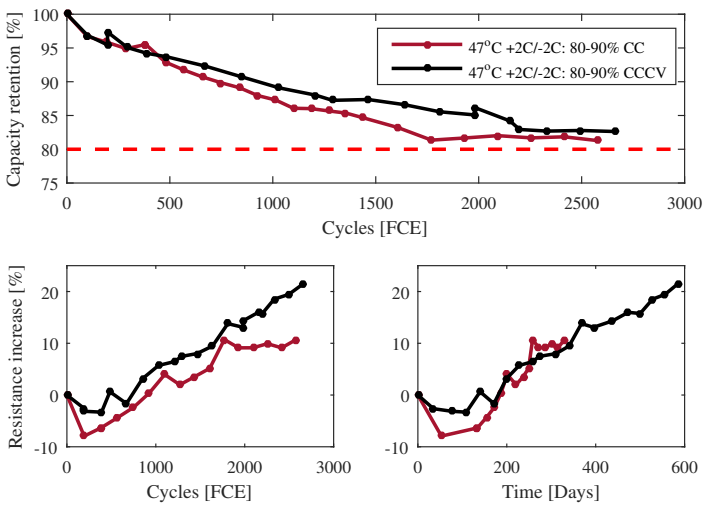

Figure 5.9: Comparison of effect of charging and discharging at high SOC with CV charging.

Again, when comparing CC with CC-CV, the cells have been subjected to different test times. The cell tested in CC-CV charging took 18 min for 1 cycle compared to 6 min for the cell tested with CC, which can have a further influence. This can be observed when the resistance is plotted as a function of days instead of FCE.

Studying the resistance as a function of FCE it might look as if the CC cell have lower resistance throughout the entire test, but if instead studying

the resistance as a function of days, it is only lower initially.

5.3.3 Effect of DOD

Larger DOD should decrease the lifetime and smaller DOD increase the lifetime [4, 5]. The smaller DOD used in the vehicle, the more dead weight will be added to the battery pack for the same amount of available energy and power. In vehicle applications, extra weight also means higher energy consumption, apart from increased cost. Accordingly, it is very important to use as large DOD as possible.

Two different DOD with CC-CV using the same upper SOC level, 0-90% and 80-90% SOC, were tested with +2C/-2C, figure 5.10. The initially stronger aging for the 10% DOD compared to the 90% DOD, again shows the effect of high SOC. Thus not only the DOD, but also the placement of the SOC interval, should be considered. Important to note is also that after middle of life (MOL) (90% SOC) the capacity retention in the 10% DOD is slowing down, while increasing for the 90% DOD. If the 10% DOD continues to follow the slower aging trend it might result in twice the lifetime of the 90% DOD.

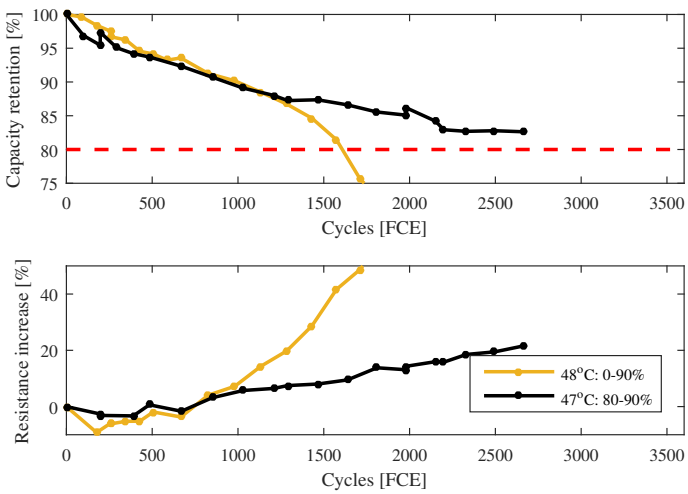

Figure 5.10: Comparison of the effect of DOD for aging using +2C/-2C in 0-90% and 80-90% SOC at 45°C.

5.4 ICA on Aged Cells

ICA was used to study the likely aging mechanism taking place in different test regimes and temperatures. Data is presented at beginning of life (BOL), MOL and EOL form cycles with 1C or C/10 rate. To see the difference between the details achieved with C/10 compared to 1C data, an initial cycle for these are shown in figure 5.11b. As the 1C data gives a less detailed picture and postmortem analysis yet is to be performed, the following is a preliminary analysis.

The 1C data also presents an issue regarding the resistance increase, to a higher extant than the C/10, making the analysis harder. The polarization from increased resistance can be removed, this has not been done and the following figures include the raw data without treatment for this.

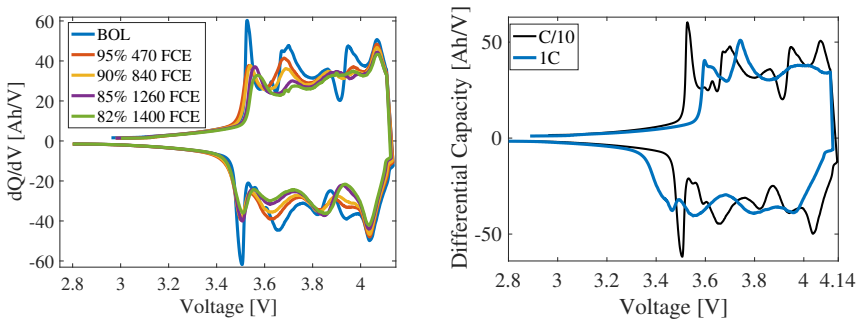

(a) (b)

Figure 5.11: ICA for a cell aged with +1C/-2C at 45°C from (a) C/10 and (b) C/10 compared to 1C cycles. See capacity curve in figure 5.7.

ICA from experimental C/10 data of a cell aged with +1C/-2C cycling at 45°C can be seen in figure 5.11a. The amplitude of the first peak from the left side is reduced by 30% from BOL and to 95% remaining capacity indicating SEI formation. The SEI formation is then progressing as the cycling goes on continuing to reduce the amplitude of the peaks and increasing the resistance. The cell becomes under discharged/charged as the resistance increases shifting the peaks to the left during charging and right during discharging.

5.4.1 Effect of Temperature Aging

That higher temperature accelerates the SEI growth can be seen from the ICA in figure 5.12, where the difference between 25 and 45 °C data is large. At 25 °C a small polarization increase can be seen over the life. This and only

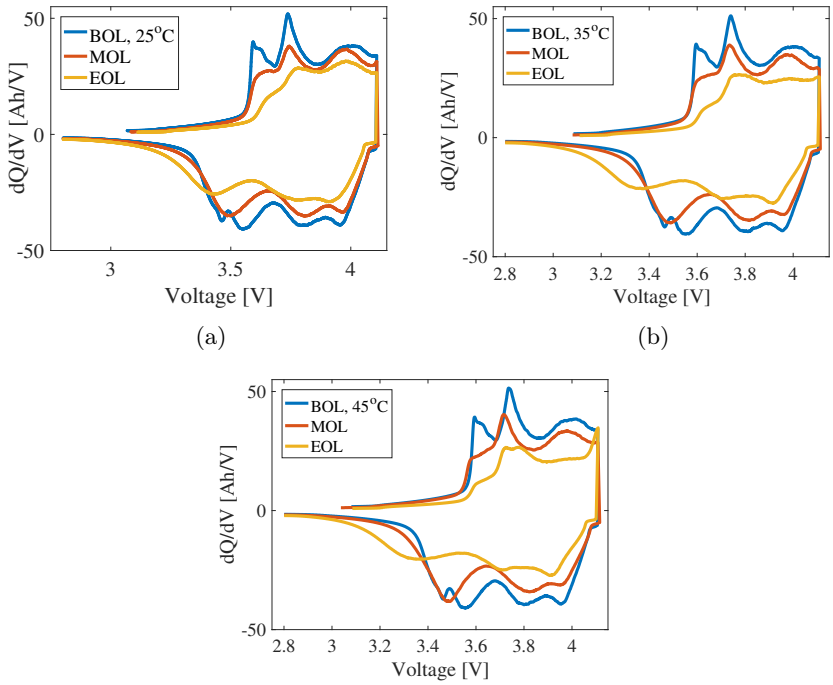

Figure 5.12: ICA from 1C data for cells aged with +2C/-2C in 0-90% SOC at (a) 25, (b) 35 and (c) 45°C ambient temperature at BOL, MOL and EOL. Capacity curves for respectively cell can be seen in figure 5.2.

a small shift of the first and middle peak to lower voltage indicate mainly loss of anode and Li^+.

The shift of these peaks toward lower voltage and the consequent loss of anode material increase with temperature. The higher temperature also results in lower amplitude of all peaks, indicating higher loss of cyclable Li^+ and thereby more SEI formation. In support, the resistance increase with temperature which is seen easiest in the ICA at the endpoints. The higher resistance gives rise to increased polarization voltage, shifting all peaks to higher or lower voltages, leading to under-charging respectively under-discharging.

There is an uneven loss of active materials observed by the middle peak in figure 5.12c being separated into two peaks at EOL. Whether there is loss of cathode material can not be said, since the loss of anode material is much larger and may conceal the former.

5.4.2 Effect of SOC Interval

The ICA for 10% intervals cycled with +2C/-2C at 35°C shows a clear trend, figure 5.13. The higher SOC interval, 60-70% SOC, shows a large loss of amplitude in all peaks in combination with a higher polarization voltage indicating loss of Li^+ and SEI formation. Strong indicators are the rapid amplitude loss of the first peak and a shift to the left of the middle peak at higher SOC.

For the middle SOC interval the first peak is visible, but shifted to a higher voltage, towards the middle peak, indicating smaller SEI formation and anode loss. The total capacity loss is less than at high SOC and a slight recovery of the capacity is seen after 2200 FCE, just after MOL. The cell has not yet reached EOL and seem to have stabilized at 85% capacity.

The low SOC interval, 10-20%, will not reach EOL within the scope of this project, maybe not even MOL. After 1500 FCE there is loss of anode material and to some extent also loss of Li^+. The cell then regains the loss of anode material, although not completely. This supports the hypothesis that anode material gets blocked or in other way hindered from participating in the cell reactions and not irreversibly lost. The cell stabilizes and very little change can be seen between 2200 and 8000 FCE.

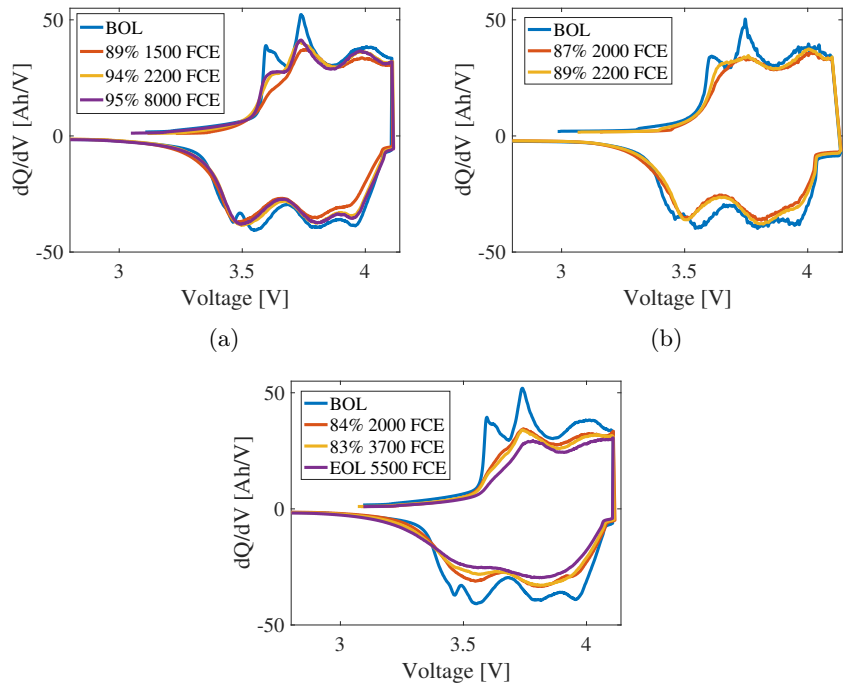

Figure 5.13: ICA from 1C data for cells aged with +2C/-2C in 10% DOD at 35°C. (a) 10-20% SOC at BOL, at a sudden capacity drop after 1500 FCE, 89%, and at 94% capacity after recovery, 2200 FCE, and at 95% after continued cycling without any further capacity loss, 7000 FCE. The cell had an average cycling temperature of 40°C. (b) 40-50% SOC at BOL, after an initial capacity drop, 87% 2000 FCE, and at 89% capacity, 2200 FCE, in a region of slower capacity retention. The cell had an average cycling temperature of 38°C. (c) 60-70% at BOL, after an initial capacity drop to, 84% 2000 FCE, and at 82% capacity, 3700 FCE, in a region of slower capacity retention, and at 80%, EOL. The cell had an average cycling temperature of 40°C. Capacity curves for the respective cells can be seen in figure 5.8b.

5.4.3 Effect of Fast Charging

Fast charging, +3C/-1C, was also included in the ICA analysis, since it showed a different aging behavior compared to the +1C/-3C cell, figure 5.4 and 5.14. Interesting is that only small differences can be seen from the ICA of the two cells. At MOL both cells have the peaks shifted to the left indicating loss of anode material. The peaks seem to be brought closer together during aging indicating that there is loss of cathode material as well. The specific cause for the reduction in amplitude is therefore hard to determine. Loss of cathode material most likely occur in combination with loss of anode material and Li^+.

The fast charged cell still maintain 3 separate peaks at EOL indicating loss of both the active materials, figure 5.14b. Between the MOL and EOL the losses seem to be mainly from SEI build up and loss of anode for both cells. The last peak has been shifted more to the left while the other peaks mainly experience a decrease in amplitude. For the +1C/-3C cell a higher resistance is observed throughout the aging indicating larger SEI formation compared to the fast charged cell. It is, however, still hard to establish whether the loss is largest on the anode or cathode side. The fast charged cell seems to have larger loss of cathode material compared to the +1C/-3C cell.

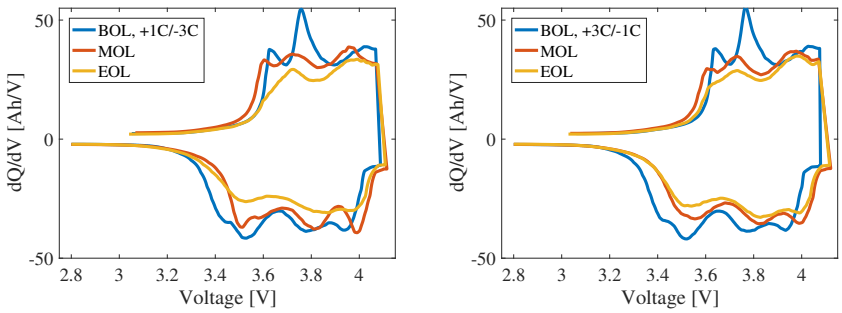

(a) (b)

Figure 5.14: ICA from 1C data for cells aged with +1C/-3C and +3C/-1C in 20-80% SOC at 40°C. (a) +1C/-3C, the cell had an average cycling temperature of 40°C. (b) +3C/-1C, the cell had an average cycling temperature of 41°C. Capacity curves for the cells can be seen in figure 5.4.

Chapter 6

Conclusions

In this thesis an extensive test matrix for commercial cells is presented together with a physics-based aging model. The results from the lifetime cycling tests showed the expected temperature dependence for 90% DOD, that higher temperature degrades the battery faster, while a different and interesting observation was made with 10% DOD. The temperature dependence had little effect within SOC intervals having a maximum lower than 50%. The expected temperature dependence could first be observed above 50% SOC and only at temperatures higher than 40°C.

When comparing the Hyzem Rural drive cycle to the synthetic CC cycle, the lifetime cycling test results showed that the Hyzem Rural drive cycle is less detrimental compared to the CC cycle with the same RMS current as C-rate.

The study also confirm that operating at high SOC levels lead to more rapid aging; only moderate aging could be observed in the low SOC intervals, while more rapid aging was noted for SOC intervals higher than 40% SOC. For 60% SOC and above that are no large differences.

Several of the 10% DOD tests in low SOC intervals showed an initial capacity drop followed by a regain and a stabilization of the capacity, thus, experiencing only minimal aging overall. The author's hypothesis is that anode material gets blocked or is in some other way reversibly hindered from participating in the cell reactions. This hypothesis is supported by the ICA made at the capacity drop and after the recovery.

Chapter 7

Future Work

During the progress of this work several phenomena have been identified that require further studies for a better understanding. Some gaps in the lifetime aging test matrix should be filled for a more complete picture.

Additional tests to investigate the cause for the initial capacity drop and sudden recovery in capacity for the 10% SOC intervals is of interest. Further more, continued testing of all 10% SOC intervals, including 30-40, 50-60% SOC, and including the so far note tested intermediate intervals, such as 35-45% SOC, should be performed. The latter in order to understand at what SOC the SEI reactions start to occur.

For a deeper understanding of the differences between the dynamic and synthetic cycles, tests with an additional synthetic CC cycle, with pauses similar to the Hyzem Rural drive cycle, is of interest. This would allow a more coherent comparison between the CC and application governed cycles.

To be able to monitor the aging with ICA during the cycling it is recommended to use data from a C/10 cycle. Therefore, changing the RPT test to include a C/10 cycle is planned for all future testing. A need to further develop test procedures to make the lifetime testing more efficient is also on the improvment list. The method for testing in small SOC intervals is to be developed to make testing more automated, but without reducing the level of control.

In order to limit the extent of lifetime tests further development of the physic-based models is needed. There are several aspects to address; determining what parameters and material properties that influence the modeled mechanism most is of high importance since parameterization of these models is a tedious task. Future work include expanding the model with temperature dependence for these key parameters.

There is little knowledge of how the different aging mechanisms are linked, to be combated by further development of the mathematical descriptions of the various aging mechanisms. The most prominent is the SEI growth and there are several publications regarding this. In this thesis the first steps were conducted in developing a physics-based aging model. The future work for the aging model is to couple the SEI growth to the loss of anode material. Also to include metal dissolution from the cathode, since LMO is known to release Mn^2+ at high potentials. As LMO only constitutes ca 30 wt% of the cathode, the capacity loss by this mechanism is likely to be small on the cathode side, although it should have an accelerating effect on the SEI growth when reaching the anode side.

Connecting the results of the aging model closer to the vehicle applications is a interesting topic that should be perused.

References

[1] European Commission, "A European Strategy for low-emission mobility," 2016. [Online]. Available: https://ec.europa.eu/clima/policies/transport_sv

[2] O. Johansson, "12 151 nya laddbara bilar i sverige 2016," 2017. [Online]. Available: http://powercircle.org/nyhet/12-151-nya-laddbara-bilar-sverige-2016/

[3] J. Voelcker, "Electric car battery warranties compared," R GreenCar-Reports, 2016. [Online]. Available: http://www.greencarreports.com/news/1107864_electric-car-battery-warranties-compared

[4] J. Groot, "State-of-Health Estimation of Li-ion Batteries: Cycle Life Test Methods," 2012, licentiatavhandling.

[5] J. Schmalstieg, S. Käbitz, M. Ecker, and D. U. Sauer, "From accelerated aging tests to a lifetime prediction model: Analyzing lithium-ion batteries," in *2013 World Electric Vehicle Symposium and Exhibition (EVS27)*, Nov 2013, pp. 1–12.

[6] E. Thomas, H. Case, D. Doughty, R. Jungst, G. Nagasubramanian, and E. Roth, "Accelerated power degradation of Li-ion cells ," *Journal of Power Sources*, vol. 124, no. 1, pp. 254 – 260, 2003.

[7] P. Ramadass, B. Haran, R. White, and B. N. Popov, "Mathematical modeling of the capacity fade of Li-ion cells ," *Journal of Power Sources*, vol. 123, no. 2, pp. 230 – 240, 2003.

[8] P. Ramadass, B. Haran, P. M. Gomadam, R. White, and B. N. Popov, "Development of First Principles Capacity Fade Model for Li-Ion Cells," *Journal of The Electrochemical Society*, vol. 151, no. 2, pp. A196–A203, 2004.

[9] R. B. Wright, C. G. Motloch, J. R. Belt, J. P. Christophersen, C. D. Ho, R. A. Richardson, I. Bloom, S. A. Jones, V. S. Battaglia, G. L. Henriksen, T. Unkelhaeuser, D. Ingersoll, H. L. Case, S. A. Rogers, and R. A. Sutula, "Calendar-and cycle-life studies of advanced technology development program generation 1 lithium-ion batteries," *Journal of power sources*, vol. 110, pp. 445–470, 08/2002 2002.

[10] J. Groot, "State-of-health estimation of li-ion batteries: Ageing models," Ph.D. dissertation, Chalmers University of Technology, 2014.

[11] G. Ning, R. White, and B. Popov, "A generalized cycle life model of rechargeable Li-ion batteries," *Electrochimica Acta*, vol. 51, pp. 2012–2022, 2006.

[12] M. Meyer, L. Komsiyska, B. Lenz, and C. Agert, "Study of the local SOC distribution in a lithium-ion battery by physical and electrochemical modeling and simulation," *Applied Mathematical Modelling*, vol. 37, no. 4, pp. 2016 – 2027, 2013.

[13] M. Doyle, T. F. Fuller, and J. Newman, "Modeling of Galvanostatic Charge and Discharge of the Lithium/Polymer/Insertion Cell," *Journal of The Electrochemical Society*, vol. 140, no. 6, pp. 1526–1533, 1993.

[14] R. Darling and J. Newman, "Modeling Side Reactions in Composite $\mathrm{LiyMn_2O_4}$ Electrodes," *Journal of The Electrochemical Society*, vol. 145, no. 3, pp. 990–998, 1998.

[15] H. Ekström and G. Lindbergh, "A Model for Predicting Capacity Fade due to SEI Formation in a Commercial Graphite/$\mathrm{LiFePO_4}$ Cell," *Journal of The Electrochemical Society*, vol. 162, no. 6, pp. A1003–A1007, 2015.

[16] R. Spotnitz, "Simulation of capacity fade in lithium-ion batteries," *Journal of Power Sources*, vol. 113, no. 1, pp. 72 – 80, 2003.

[17] H. D. Abruña, Y. Kiya, and J. C. Henderson, "Batteries and electrochemical capacitors," *Physics Today*, vol. 61, no. 12, pp. 43–47, 2008.

[18] H. Berg, *Batteries for Electric Vehicles, Materials and Electrochemistry*. Cambridge University Press, 2015.

[19] J. Vetter, P. Novák, M. Wagner, C. Veit, K.-C. Möller, J. Besenhard, M. Winter, M. Wohlfahrt-Mehrens, C. Vogler, and A. Hammouche, "Ageing mechanisms in lithium-ion batteries," *Journal of Power Sources*, vol. 147, no. 1–2, pp. 269 – 281, 2005.

[20] M. Winter, J. O. Besenhard, M. E. Spahr, and P. Novák, "Insertion Electrode Materials for Rechargeable Lithium Batteries," *Advanced Materials*, vol. 10, no. 10, pp. 725–763, 1998.

[21] C.-H. Doh, B.-C. Han, B.-S. Jin, and H.-B. Gu, "Structures and Formation Energies of Li_xC_6 (x=1-3) and its Homologues for Lithium Rechargeable Batteries," *Bulletin of the Korean Chemical Society*, vol. 32, no. 6, pp. 2045 – 2050, 2011.

[22] M. M. Doeff, *Encyclopedia of Sustainability Science and Technology, Chapter 2 Battery Cathodes*, R. A. Meyers, Ed. Springer-Verlag New York, 2012.

[23] V. Agubra and J. Fergus, "Lithium ion battery anode aging mechanisms," *Materials*, vol. 6, no. 4, pp. 1310–1325, 2013.

[24] M. Klett, "Electrochemical Studies of Aging in Lithium-Ion Batteries," Ph.D. dissertation, Royal Institute of Technology, 2014.

[25] G. K. Prasad and C. D. Rahn, "Model based identification of aging parameters in lithium ion batteries," *Journal of Power Sources*, vol. 232, pp. 79 – 85, 2013.

[26] T. Granerus, Volvo Cars, Personal communication.

[27] J. Bates and D. Leibling, "Spaced out perspectives on parking policy," Royal Automobile Club Foundation for Motoring, 2012. [Online]. Available: http://www.racfoundation.org/assets/rac_foundation/content/downloadables/spaced_out-bates_leibling-jul12.pdf

[28] S. Käbitz, J. B. Gerschler, M. Ecker, Y. Yurdagel, B. Emmermacher, D. André, T. Mitsch, and D. U. Sauer, "Cycle and calendar life study of a graphite|LiNi1/3Mn1/3Co1/3O2 Li-ion high energy system. Part A: Full cell characterization," *Journal of Power Sources*, vol. 239, pp. 572 – 583, 2013.

[29] D. H. Jang, Y. J. Shin, and S. M. Oh, "Dissolution of Spinel Oxides and Capacity Losses in 4V Li/Lix Mn_2O_4 Cells," *Journal of The Electrochemical Society*, vol. 143, no. 7, pp. 2204–2211, 1996.

[30] L. Yang, M. Takahashi, and B. Wang, "A study on capacity fading of lithium-ion battery with manganese spinel positive electrode during cycling," *Electrochimica Acta*, vol. 51, no. 16, pp. 3228–3234, 2006.

[31] K. C. Högström, "The Complex Nature of the Electrode/Electrolyte Interfaces in Li-ion Batteries," Ph.D. dissertation, Uppsala University, 2014.

[32] M. Dubarry, C. Truchot, B. Y. Liaw, K. Gering, S. Sazhin, D. Jamison, and C. Michelbacher, "Evaluation of commercial lithium-ion cells based on composite positive electrode for plug-in hybrid electric vehicle

applications. Part II. Degradation mechanism under 2 C cycle aging," *Journal of Power Sources*, vol. 196, pp. 10 336–10 343, 2011.

[33] S. Malmgren, K. Ciosek, M. Hahlin, T. Gustafsson, M. Gorgoi, H. Rensmo, and K. Edström, "Comparing anode and cathode electrode/electrolyte interface composition and morphology using soft and hard X-ray photoelectron spectroscopy ," *Electrochimica Acta*, vol. 97, pp. 23 – 32, 2013.

[34] K. Edström, T. Gustafsson, and J. Thomas, "The cathode–electrolyte interface in the Li-ion battery," *Electrochimica Acta*, vol. 50, no. 2–3, pp. 397 – 403, 2004.

[35] S. J. An, J. Li, C. Daniel, D. Mohanty, S. Nagpure, and D. L. W. III, "The state of understanding of the lithium-ion-battery graphite solid electrolyte interphase (SEI) and its relationship to formation cycling," *Carbon*, vol. 105, pp. 52 – 76, 2016.

[36] P. Horsman, *Comprehensive Treatise of Electrochemistry, Vol. 6: Electrodics - Transport: Chapter 1 and 2.* Plenum Press, 1983.

[37] N. Nitta, F. Wu, J. T. Lee, and G. Yushin, "Li-ion battery materials: present and future," *Materials Today*, vol. 18, no. 5, pp. 252 – 264, 2015.

[38] D. Aurbach, A. Zaban, Y. Ein-Eli, I. Weissman, O. Chusid, B. Markovsky, M. Levi, E. Levi, A. Schechter, and E. Granot, "Recent studies on the correlation between surface chemistry, morphology, three-dimensional structures and performance of Li and Li-C intercalation anodes in several important electrolyte systems," *Journal of Power Sources*, vol. 68, no. 1, pp. 91 – 98, 1997.

[39] B. Tjaden, S. J. Cooper, D. J. Brett, D. Kramer, and P. R. Shearing, "On the origin and application of the bruggeman correlation for analysing transport phenomena in electrochemical systems," *Current Opinion in Chemical Engineering*, vol. 12, pp. 44 – 51, 2016.

[40] T. G. Zavalis, "Mathematical Models for Investigation of Performance, Safety, and Aging in Lithium-Ion Batteries," Ph.D. dissertation, KTH, Applied Electrochemistry, 2013.

[41] T. Danner, M. Singh, S. Hein, J. Kaiser, H. Hahn, and A. Latz, "Thick electrodes for Li-ion batteries: A model based analysis," *Journal of Power Sources*, vol. 334, pp. 191 – 201, 2016.

[42] E. Wikner, J. Lesser, and T. Thiringer, "Accelerated lifetime testing in small SOC intervals on commercial pouch cells, challenges and countermeasures," 2017, EPE'17 ECCE Europe.

[43] T. Grube, *Fuel Cells : Data, Facts and Figures, Chapter 2 Passenger Car Drive Cycles*, D. N. G. Prof. Detlef Stolten, Dr. Remzi C. Samsun, Ed. Wiley-VCH Verlag GmbH Co. KGaA, 2016.

[44] M. Dubarry, B. Y. Liaw, M.-S. Chen, S.-S. Chyan, K.-C. Han, W.-T. Sie, and S.-H. Wu, "Identifying battery aging mechanisms in large format Li ion cells," *Journal of Power Sources*, vol. 196, no. 7, pp. 3420 – 3425, 2011.

[45] M. D. Levi and D. Aurbach, "Simultaneous Measurements and Modeling of the Electrochemical Impedance and the Cyclic Voltammetric Characteristics of Graphite Electrodes Doped with Lithium," *The Journal of Physical Chemistry B*, vol. 101, no. 23, pp. 4630–4640, 1997.

[46] T. Ohzuku, Y. Iwakoshi, and K. Sawai, "Formation of LithiumGraphite Intercalation Compounds in Nonaqueous Electrolytes and Their Application as a Negative Electrode for a Lithium Ion (Shuttlecock) Cell," *Journal of The Electrochemical Society*, vol. 140, no. 9, pp. 2490–2498, 1993.

[47] S.-h. Wu and P.-H. Lee, "Nonlinear Cycling Aging of a Commercial 18650 Lithium Ion Cell," *Meeting Abstracts*, vol. MA2016-03, no. 2, p. 1198, 2016.

[48] I. Buchberger, S. Seidlmayer, A. Pokharel, M. Piana, J. Hattendorff, P. Kudejova, R. Gilles, and H. A. Gasteiger, "Aging Analysis of Graphite/LiNi1/3Mn1/3Co1/3O2 Cells Using XRD, PGAA, and AC Impedance," *Journal of The Electrochemical Society*, vol. 162, no. 14, pp. A2737–A2746, 2015.

[49] T. Ohzuku, M. Kitagawa, and T. Hirai, "Electrochemistry of Manganese Dioxide in Lithium Nonaqueous Cell: III XRay Diffractional Study on the Reduction of SpinelRelated Manganese Dioxide," *Journal of The Electrochemical Society*, vol. 137, no. 3, pp. 769–775, 1990.

[50] N. Leifer, F. Schipper, E. M. Erickson, C. Ghanty, M. Talianker, J. Grinblat, C. M. Julien, B. Markovsky, and D. Aurbach, "Studies of Spinel-to-Layered Structural Transformations in LiMn2O4 Electrodes Charged to High Voltages," *The Journal of Physical Chemistry C*.

[51] A. Nyman, M. Behm, and G. Lindbergh, "Electrochemical characterisation and modelling of the mass transport phenomena in $LiPF_6$–EC–EMC electrolyte," *Electrochimica Acta*, vol. 53, no. 22, pp. 6356 – 6365, 2008.

[52] Y. Wang, S. Nakamura, M. Ue, and P. B. Balbuena, "Theoretical Studies to Understand Surface Chemistry on Carbon Anodes for Lithium-Ion

Batteries: Reduction Mechanisms of Ethylene Carbonate," *Journal of American Chemical Society*, vol. 123, p. 11708, 2001.

[53] D. Aurbach, M. D. Levi, E. Levi, and A. Schechter, "Failure and Stabilization Mechanisms of Graphite Electrodes," *Journal of Physical Chemistr B*, vol. 101, p. 2195, 1997.

[54] C. R. Yang, Y. Y. Wang, and C. C. Wan, "Composition Analysis of the Passive Film on the Carbon Electrode of a Lithium-Ion Battery with an EC-Based Electrolyte," *Journal of Power Sources*, vol. 72, p. 66, 1998.

[55] S.-P. Kim, A. C. T. van Duin, and V. B. Shenoy, "Effect of Electrolytes on the Structure and Evolution of the Solid Electrolyte Interphase (SEI) in Li-Ion Batteries: A Molecular Dynamics Study," *Journal of Power Sources*, vol. 196, p. 8590, 2011.

[56] K. Tasaki, A. Goldberg, J.-J. Lian, M. Walker, A. Timmons, and S. J. Harris, "Solubility of Lithium Salts Formed on the Lithium-Ion Battery Negative Electrode Surface in Organic Solvents," *Journal Electrochemistry Society*, vol. 156, p. A1019, 2009.

[57] A. M. Andersson, M. Herstedt, A. G. Bishop, and K. Edström, "The Influence of Lithium Salt on the Interfacial Reactions Controlling the Thermal Stability of Graphite Anodes," *Electrochimica Acta*, vol. 47, p. 1885, 2002.

[58] K. Ciosek Högström, S. Malmgren, M. Hahlin, H. Rensmo, F. Thébault, P. Johansson, and K. Edström, "The Influence of PMS-Additive on the Electrode/Electrolyte Interfaces in LiFePO4/Graphite Li-Ion Batteries," *The Journal of Physical Chemistry C*, vol. 117, no. 45, pp. 23 476–23 486, 2013.

[59] S.-L. Wu, W. Zhang, X. Song, A. K. Shukla, G. Liu, V. Battaglia, and V. Srinivasan, "High Rate Capability of Li(Ni1/3Mn1/3Co1/3)O2 Electrode for Li-Ion Batteries," *Journal of The Electrochemical Society*, vol. 159, no. 4, pp. A438–A444, 2012.